Simulation of blood flows in a stenosed and bifurcating artery using Finite Volume Methods and OpenFOAM

BY

Sunitha Nagarathnam

A thesis submitted for the degree of

Doctor of Philosophy

in the Department of Mathematics and Applied Mathematics,
Faculty of Science, University of Cape Town
February 2022

Supervisor: Dr. Tiri CHINYOKA
Department of Mathematics and Applied Mathematics, and
Center for Research in Computational and Applied Mechanics,
University of Cape Town.

Declaration

I, the undersigned, Sunitha Nagarathnam, hereby declare that the work contained in this thesis titled "Simulation of blood flows in a stenosed and bifurcating artery using Finite Volume Methods and OpenFOAM", is my original work, and that any work done by others or by myself previously has been acknowledged and referenced accordingly and that it has not been and will not be used to pursue or attain any other academic degree of any level at any other academic institution, be it foreign or South African.

Signature: Signed by candidate

Date : 15/06/2022

Dedication

To my son and daughter, Prithiv and Maanvitha, my father and mother, Nagarathnam and Parvathi.

Acknowledgements

I would like to thank my supervisor, Dr. Tiri Chinyoka, for giving me opportunity of immersing myself in the numerical computation and software simulation tools. Thank you for your passionate, confidence, optimism and patience throughout these years in the field of numerical computation. I would also like to thank the Center for High Performance Computing (CHPC) in Cape Town for allowing us to use their high performance computing facilities and I would especially like to thank Dr. Andrew Gill from the CHPC for his availability and assistance in OpenFOAM.

It should be acknowledged that this work has been made possible by the financial contributions from the South African Research Chair in Computational Mechanics via Professor Daya Reddy. I am grateful for these funding contributions towards my PhD programme.

Finally, I would like to deeply say thank you to my husband, for always believing in me.

Contents

Abstract

Numerical simulations of the complex flows of complex (viscoelastic) fluids are investigated. The primary fluid investigated in this thesis is human blood, a complex fluid which can be modelled via viscoelastic constitutive models. The most commonly used constitutive models for viscoelastic fluids include the Oldroyd-B, Giesekus, Johnson-Segalman, Finitely Extensible Non-Linear Elastic (FENE), Phan-Thein-Tanner (PTT) models etc. Our Numerical approach is based on the finite volume methods implemented on the OpenFOAM platform. We employ the Giesekus, Oldroyd-B, and Generalized Oldroyd-B viscoelastic constitutive models in this thesis, depending on the underlying context. Numerical validation of our results is conducted via the most used benchmark flow problems for viscoelastic fluid flow. The robust and efficient numerical methodologies are then deployed to investigate the flow characteristics, and hence illustrate various novel behavior, for blood flow in stenosed and bifurcated arteries.

The present work took advantage of the availability of a reasonable set of viscoelastic constitutive model solvers within OpenFOAM, specifically the *viscoelasticFluidFoam* solver which we modified and developed to suit our focused needs for blood flow computations. The modified computational algorithms were successfully validated against well-known benchmark flow problems in the literature. Noting that the Giesekus viscoelastic constitutive model is a generalization of both the Oldroyd-B and Generalized Oldroyd-B models, the validation of results is carried out via the Giesekus model enabling us to develop a general-purpose code capable of simulating several viscoelastic constitutive models. The main results were otherwise presented for the Oldroyd-B and Generalized Oldroyd-B models as these are the most applicable to blood flow modelling. The results demonstrate that the velocity spurt through the stenosis is directly proportional to the constriction caused by the stenosis. The

higher the blockage from the constriction, the higher the corresponding velocity spurt through the constriction. This velocity behavior, as the constriction blockage increases, correspondingly increase the wall shear stresses. High wall shear stresses significantly increase the possibility of rupture of the stenosis/blockage. This can lead to catastrophic consequences in the usual case where the stenosis is caused by tumor growth.

Keywords:

Blood flow, Stenosed and bifurcating artery, Viscoelastic fluid, Oldroyd-B model, Generalized Oldroyd-B model, Giesekus Model, Numerical Simulation, Finite volume methods, OpenFOAM.

List of Tables

List of Figures

Chapter 1

Introduction

1.1 Background and Objectives

Non-Newtonian fluid behaviour is characterized in at least three ways; the Generalized Newtonian Fluids; viscoelastic fluids; or a combination of the two [1, 2]. Generalized Newtonian Fluids do not follow Newton's law of viscosity, their viscosity therefore depends on prevailing shear-rates. The viscosity of Newtonian fluids on the other hand is unaffected by prevailing shear rates and hence remains constant even when the shear-rates vary widely in a particular flow set-up. Most paints for example, become runnier when shaken (i.e., when exposed to higher shear-rates) and are thus examples of Generalized Newtonian Fluids. Many salt solutions and molten polymers exhibit Generalized Newtonian Fluid behaviour, as do many commonly found substances such as custard, honey, toothpaste, starch suspensions, corn starch, paint, blood, melted butter, and shampoo, [3].

Generalized Newtonian Fluid behaviour mostly manifests as shear-thinning behaviour, in which the fluid viscosity decreases with increasing shear-rates. For some lower viscosity non-Newtonian fluids, the flow can be transitional or become turbulent

under expected operating conditions. For suspension transport in a pipe for example, it is advantageous to operate in a transitional regime because this results in the lowest energy consumption [4, 5, 6]. Despite the practical importance, the understanding of transition and turbulence in shear- thinning fluids is still not well understood. More advanced computational techniques and methodologies would yet need to be developed to better resolve and understand transition and turbulence in wall-bounded flows of shear-thinning fluids. Experiments can provide an accurate description of non-Newtonian flow behaviour but it can be difficult to design appropriate laboratory fluids in which the rheological properties can be adjusted as needed. In addition, certain degree of elastic behaviour may be present in some polymer additives which complicate the physics of the fluids [6].

The majority of polymeric fluids exhibit both viscous (fluid) and elastic (solid) behaviour and are termed viscoelastic fluids [1, 2]. The elastic behaviour results in the phenomena of fading memory for viscoelastic fluids, phenomena which is readily demonstrated in recoil experiments [1, 2]. The elastic behaviour of viscoelastic fluids is subsequently characterized by time constants known as the relaxation times and the retardation times. Viscoelastic fluids may either have constant shear-viscosity as with Newtonian fluids, such viscoelastic fluids fall under the class of Boger fluids [40]. Additionally viscoelastic fluids may exhibit non-constant shear-viscosity as with the Generalized Newtonian Fluids. We shall call such fluids the Generalized Viscoelastic Fluids.

This thesis focuses on blood flow simulations. Blood has been experimentally demonstrated to fall under the category of Generalized Viscoelastic Fluids [4]. Several investigations have been conducted with blood being modelled either as a Generalized Newtonian Fluid or as a Boger-type viscoelastic fluid. This thesis will run comparative simulations using both the viscoelastic and generalized viscoelastic fluid models. The

elastic behavior of blood is now well documented and hence the modelling of blood via purely viscous fluid models has been conclusively demonstrated to be inadequate [4]. Purely viscous (i.e., Generalized Newtonian Fluid) models for blood will therefore not be considered in this thesis.

The viscous/elastic properties of blood are governed by the prevailing shear-rates and the concentration of red blood cells in the blood [4]. The elastic behavior increases rapidly with increasing hematocrit level as direct cell-to-cell interactions become more probable. While the viscous and elastic components of the shearing stress are linearly related to the velocity gradient at low gradients, they become nonlinearly related at high gradients. At low haematocrit levels the blood properties are mainly attributed to the diffuse and non-interacting red cells suspended in the plasma. Under these conditions, the elastic property is out of the range of present measurement techniques. The viscous property of the red cell, however, is clearly measurable and is thought to be strongly influenced by the cell's deformability. These new observations are discussed in the light of other contemporary work on the structure and flow properties of blood.

The primary objectives of the thesis can be summarized as follows:

- To develop viscoelastic constitutive models for blood flowing in an artery. Specifically, the Oldroyd-B and Generalized Oldroyd-B viscoelastic constitutive models will be considered.

- To develop robust and efficient numerical and computational methodologies for the simulation of blood flow in an artery, specifically, a bifurcating artery that additionally has a stenosis. The numerical algorithms will be developed to resolve the mathematical model equations arising out of the more general Giesekus viscoelastic constitutive model.

- To explore the effects of shear-viscosity modelling of blood via a comparative analysis of the result from the Oldroyd-B (constant shear-viscosity) and Generalized Oldroyd-B (variable shear-viscosity) viscoelastic constitutive models.

- To lay the groundwork for the modelling and analysis of blood-concentration related ailments (such as diabetes) as well as the blood-temperature related ailments (such as rheumatic fever). The earlier will involve the inclusion of (say blood-sugar) concentration models to the model equations presented in this thesis and the latter will involve the addition of the energy equation as is done, say, in [18, 19, 17], etc.

1.2 Blood Components

Blood is a specialized and complex body fluid whose components are responsible for the non-Newtonian character of the blood, specifically, the variable shear-viscosity and the elastic behaviour [4, 7, 8, 9, 10]. Blood has four (4) main components: blood plasma, red blood cells, white blood cells, and blood platelets. Blood plasma constitutes that liquid part of blood and the remaining three components (red blood cells, white blood cells, and blood platelets) constitute the solid phase. The liquid part, blood plasma, is a mixture of water, salts, and protein. Over fifty percent (50%) of human blood is plasma, [11].

Red blood cells (RBC) primarily deliver oxygen from the lungs to the internal tissues and organs. White blood cells (WBC) fight infection and are part of the body's immune system. Blood platelets help blood to clot in response to cuts and wounds. Both types of blood cells, the RBC and the WBC, are made in the bone marrow, the spongy material filling the hollow interior of bones. Healthy bone marrow is therefore of critical importance to the sustenance of life, this especially considering

that the blood cells, RBC and WBC, naturally have a short life span and would need to be replenished regularly. Red blood cells have a lifespan of about one hundred and twenty (120) days, some white blood cells may live for less than a day, but others do survive for much longer. As with the blood cells, blood platelets also have a relatively short lifespan of about six (6) days, [12].

Human life, as with that of all mammals, can only be sustained if a certain amount of blood is circulating within the blood vessels (such as capillaries, arteries, and veins) and internal organs (such as the hearts, brain, lungs, kidneys, liver, etc.). As mentioned earlier, whole blood is a mixture of liquid and solid components, specifically about 55% percent plasma and 45% blood cells and platelets [14]. The volume of blood varies per individual depending on age, weight, gender, etc. An average-sized man would have about twelve (12) pints of blood in their body whereas an average-sized woman would have about nine pints of blood in their circulatory system. Given its volume within the body, blood constitutes between 7-8% of the human body weight [4, 7, 8, 9, 10, 14].

Blood is a vital transport medium (for life sustaining elements) among the various internal organs. In addition to being the primary medium of transport of life-sustaining elements within the body, blood also sustains via other properties, such as its ability to clot when exposed to foreign environments. The multiple different functions of blood within the body can be summarized as, [13]:

- transporting oxygen and important nutrients to the lungs and tissues;
- forming blood clots around cuts and wounds to prevent excess blood loss;
- transporting cells (specifically the WBC) and antibodies around the circulatory system and internal organs to fight infection;

- transporting waste products to the kidneys and liver, hence ensuring an internal filtration and delf-cleansing process for the blood;
- regulating internal body temperature and ensuring that this remains within the required ranges for the internal organs to function.

1.2.1 Specific functions of blood components

Figure 1.1, adopted from [14] gives a representative picture of the liquid (plasma) and solid (blood cells and platelets) components of blood.

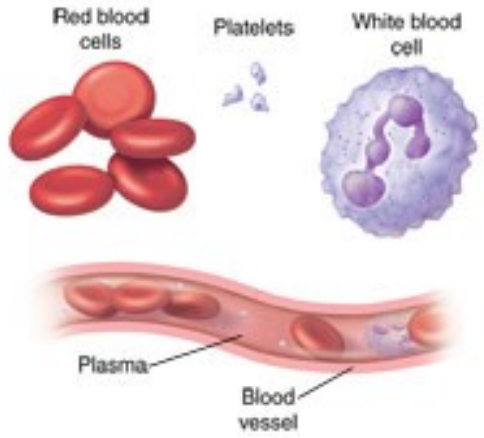

Figure 1.1: Pictorial of blood composition; liquid/solid components [14].

As already mentioned, the liquid component of blood is called plasma, a mixture of water, sugar, fat, protein, and salts. Blood plasma is a yellowish fluid whose main function is to serve as the transport medium throughout the circulatory system and internal organs. Specifically, the blood plasma transports the blood cells and platelets, and hence also oxygen, carbon dioxide, nutrients, waste products, antibodies, clotting proteins, chemical messengers such as hormones, proteins, etc.

Red blood cells, also known as erythrocytes, are the most between the two blood cell types. They are the primary means of oxygen transport from the lungs to the internal

organs and tissues and also the primary means of carbon dioxide transport from the organs/tissues back to the lungs from where it is expelled from the body. Given their huge prevalence, being overwhelmingly the most common of the blood cells by far, the red blood cells therefore give whole blood its distinctive red colour.

White blood cells are by far much fewer in number than the red blood cells, accounting for about 1 percent of human blood. Their primary function is to protect against infection. The most common type of white blood cells, accounting for between 55-70% of the total white blood cell count, are called the neutrophils. The neutrophils are effectively rapid response cells with regards to body infections and they have a very short lifespan, surviving for less than a day on average. This therefore brings into sharp focus, the importance of bone marrow, which must work to constantly replenish the neutrophils so that the body's rapid response abilities against infection are not compromised. Specifically, even though blood transfusion would help replenish in real time other types of blood cells, mainly the red blood cells, it (transfusion) would be largely ineffective as a means of replenishing neutrophils given their very short lifespan – the need for healthy bone marrow can therefore not be overstated, [15, 16].

The remaining type of white blood cells (known as the lymphocytes) exist in two forms; T-lymphocytes, which help regulate the immune responses of the body and are responsible for directly attacking tumors and infected cells; and B-lymphocytes, whose function is to make antibodies, i.e., proteins that specifically target bacteria, viruses, etc.

Unlike red and white blood cells, blood platelets are not actually cells per-se but rather small fragments of cells. Blood platelets help in the blood clotting (or coagulation) process by gathering at the site of a wound or injury, sticking to the lining of the injured blood vessel, and forming a platform on which blood coagulation can occur. This results in the formation of a fibrin clot, which covers the wound and prevents

blood from leaking out. Fibrin also forms the initial scaffolding upon which new tissue forms, thus promoting healing.

1.3 Conservation Equations

In this thesis, we consider blood as an incompressible fluid and hence the density of the blood (ρ) will be assumed constant. The thesis also investigates blood flow in a section of an artery and hence we also assume constant blood concentration and constant blood temperature. As cited under the objectives, the thesis nonetheless lays the groundwork for the modelling and analysis of blood-concentration related ailments (such as diabetes) as well as the blood-temperature related ailments (such as rheumatic fever). The earlier will involve the inclusion of (say blood-sugar) concentration models to the model equations presented in this thesis and the latter will involve the addition of the energy equation as is done for other non-isothermal viscoelastic flow applications, say, in [17, 18, 19, 20, 21, 22].

Under the given assumptions, the governing equations for the blood velocity are those derived from mass-conservation, Eq. (1.1), and momentum-conservation, Eq. (1.2),

$$\nabla \cdot \boldsymbol{v} = 0 \tag{1.1}$$

$$\rho \left(\frac{\partial \boldsymbol{v}}{\partial t} + \nabla \cdot (\boldsymbol{v}\,\boldsymbol{v}) \right) = -\nabla p + \nabla \cdot \boldsymbol{\sigma}. \tag{1.2}$$

In Eqs. (1.1) and (1.2), $\boldsymbol{v}$ represents the blood velocity, which will be considered 2D in this thesis with components in the x- and y- directions, t represents time, p is the pressure field and $\boldsymbol{\sigma}$ represents the total stress tensor. Specifically,

$$\boldsymbol{\sigma} = 2\eta \boldsymbol{S} + \boldsymbol{\tau}, \tag{1.3}$$

where $\boldsymbol{S}$ denotes the deformation-rate tensor,

$$\boldsymbol{S} = \frac{1}{2}\left[\nabla \boldsymbol{v} + (\nabla \boldsymbol{v})^T\right],$$

with shear-viscosity η. The polymer-stress tensor $\boldsymbol{\tau}$ would be described by an appropriate and empirically determined polymer-stress constitutive-model, which we will alternatively refer to as the viscoelastic constitutive model.

1.4 Viscoelastic Constitutive Models

The flow dynamics of all Newtonian fluids, such as water, are described via the Navier-Stokes equations, irrespective of the specific fluid! In particular, all deformation processes for Newtonian fluids can be sufficiently described via the deformation-rate tensor once the constant shear-viscosity (η) of the fluid is known.

This is sadly not the case for polymeric (viscoelastic) fluids. Each viscoelastic fluid would needs its own specific stress constitutive model to describe the deformation processes for the specific fluid. Empirical viscoelastic constitutive models (for the polymeric stress tensor $\boldsymbol{\tau}$) must therefore be developed/determined for each viscoelastic fluid.

A number of viscoelastic constitutive models have been developed for a wide range of viscoelastic fluids.

1.4.1 Maxwell and Jeffrey Models

These are the simplest viscoelastic constitutive models developed from spring/dashpot analogies of the polymer molecules [1, 2], see Fig. 1.2.

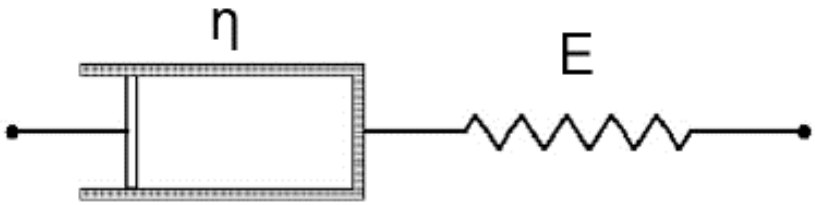

Figure 1.2: Maxwell models of polymer molecules are analogous spring-dashpot models.

The combination of the elastic spring and viscous dashpot would essentially provide the basis for the description of the analogous elastic/viscous behavior of the fluid. In particular, the polymeric-stress tensor ($\boldsymbol{\tau}$) for the fluid is then obtained by combining the physical and analogous laws for the spring and dashpot arrangement (Hooke's Law etc.),

$$\boldsymbol{\tau} + \lambda \frac{\partial \boldsymbol{\tau}}{\partial t} = 2\eta \boldsymbol{S}, \tag{1.4}$$

where λ is a relaxation time, specific to the fluid under consideration. Eq. (1.4) represents a linear system of first order Partial Differential Dquations (PDEs) and a general solution, see Eq. (1.5), can be readily found for constant λ,

$$\boldsymbol{\tau} = \int_{-\infty}^{t} G(\hat{t})\, \boldsymbol{S}(\hat{t})\, d\hat{t}, \tag{1.5}$$

where,

$$G(\hat{t}) = 2\frac{\eta}{\lambda} \exp\left(\frac{t-\hat{t}}{\lambda}\right),$$

is a relaxation modulus, [1, 2]. The Jeffrey model [1, 2] is a modification of the Maxwell model to incorporate a retardation time in addition to the relaxation time. The corresponding spring-dashpot model for a Jeffrey fluid is illustrated in Fig. 1.3.

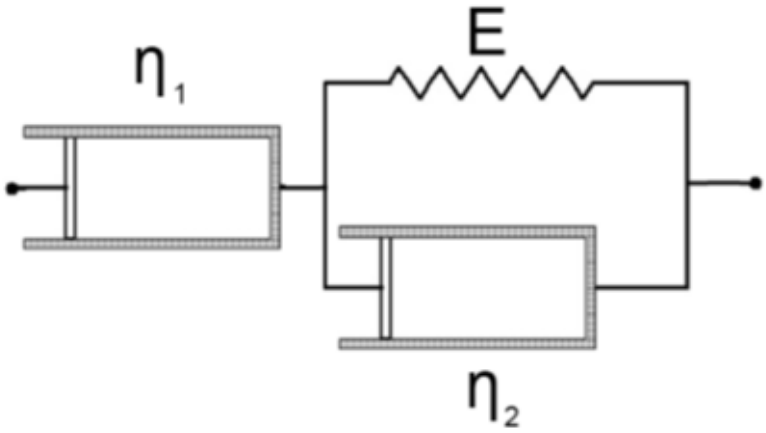

Figure 1.3: Spring-dashpot model for a Jeffrey fluid.

The stress constitutive model for a Jeffrey fluid is given in Eq. (1.6),

$$\boldsymbol{\tau} + \lambda_1 \frac{\partial \boldsymbol{\tau}}{\partial t} = 2\eta_T \left(\boldsymbol{S} + \lambda_2 \frac{\partial \boldsymbol{S}}{\partial t} \right), \tag{1.6}$$

where $\eta_T = \eta_1 + \eta_2$ is the total, λ_1 is a relaxation time, and λ_2 is a retardation time. The Maxwell and Jeffrey models essentially describe the behaviour os a single polymer molecule. These models can therefore be generalized to consider an infinite number of polymer molecules so as to closely resemble polymeric fluids,

$$\boldsymbol{\tau} = \sum_{k=1}^{\infty} \boldsymbol{\tau}_k,$$

with $\boldsymbol{\tau}_k$ described either by the Maxwell or Jeffrey model. This leads to either the Generalized Maxwell model or respectively the Generalized Jeffrey model.

The Maxwell and Jeffrey models, or their Generalized version are all linear PDEs and hence are incapable of describing important nonlinear viscoelastic phenomena. The development of nonlinear viscoelastic constitutive models is therefore of fundamental importance given the industrial, commercial, and domestic significance and applications of nonlinear viscoelastic phenomena.

Examples of nonlinear viscoelastic constitutive models include, the Oldroyd-B model, Generalized Oldroyd-B model, Giesekus model, Johnson-Segalman model, Phan-Thien-Tanner model, Rolie-Poly model, etc., for more details, we refer to the sample references [1, 2, 23, 24, 25, 26, 27].

1.4.2 Oldroyd-B model

The mixture of a polymer and a solvent would lead to a polymer solution whose properties are determined by the constituent polymer and solvent components. The total stress tensor, $\boldsymbol{\tau}$, can therefore be split into a polymer, $\boldsymbol{\tau}_p$, and a solvent, $\boldsymbol{\tau}_s$ component. The solvent stress is purely viscous (Newtonian) and hence is fully described by the Newton's law of deformation, Eq. (1.7). The polymer stress satisfies a nonlinear constitutive equation, Eq. (1.8).

$$\boldsymbol{\tau}_s = 2\eta_s \boldsymbol{S}, \tag{1.7}$$

$$\boldsymbol{\tau}_p + \lambda \overset{\nabla}{\boldsymbol{\tau}}_p = 2\eta_p \boldsymbol{S}, \tag{1.8}$$

$$\boldsymbol{\tau} = \boldsymbol{\tau}_s + \boldsymbol{\tau}_p, \tag{1.9}$$

where η_s and η_p are the solvent and polymer viscosities respectively and the total viscosity is,

$$\eta_T = \eta_s + \eta_p.$$

Eqs. (1.7) through (1.8) can be combined to given a single equation, see Eq. (1.10), for the total stress tensor, $\boldsymbol{\tau}$, of the Oldroyd-B fluid,

$$\boldsymbol{\tau} + \lambda_1 \overset{\nabla}{\boldsymbol{\tau}} = 2\eta_T \left(\boldsymbol{S} + \lambda_2 \overset{\nabla}{\boldsymbol{S}} \right), \tag{1.10}$$

where, as before, $\lambda_1 = \lambda$ is a relaxation time and λ_2 is a retardation time. Taking $\eta_p = 0$ reduces the Oldroyd-B model to the Upper Convective Maxwell (UCM) model. Taking $\eta_p = \lambda_1 = \lambda_2 = 0$ reduces the Oldroyd-B model to a (viscous) Newtonian fluid.

The Oldroyd-B fluid belongs to the of Boger fluids, viscoelastic fluids which exhibit constant shear-viscosity. the modification to non-constant shear-viscosity leads to the Generalized Oldroyd-B model.

1.4.3 Generalized Oldroyd-B model

Robust experimental investigations have conclusively demonstrated that blood exhibits non-constant shear-viscosity, see for example [28, 29]. Specifically, the viscosity of blood, as with that of many other non-Newtonian fluids, depends on prevailing shear-rates,

$$\eta = \eta(\dot{\gamma}), \quad \text{with}, \dot{\gamma} = \sqrt{2\boldsymbol{S} : \boldsymbol{S}^T}. \tag{1.11}$$

The appropriate viscosity constitutive models for $\eta(\dot{\gamma})$ are obtained empirically, e.g the Cross model, [30, 31],

$$\eta(\dot{\gamma}) = \eta_\infty + (\eta_0 - \eta_\infty)\left[\frac{1}{1+(\varepsilon\,\dot{\gamma})^m}\right]^b, \tag{1.12}$$

More information about blood viscosity models can be found for example in [29, 41]. Blood is a shear-thinning fluid and hence, for blood flow modelling, the parameters m and b in Eq. (1.12) must be non-negative; $b \geq 0$ and $m \geq 0$.

A Generalized Oldroyd-B model with appropriate shear-thinning viscosity, $\eta(\dot{\gamma})$, [32, 33, 34, 35, 36, 37] for blood flow modelling captures the intrinsic rheological behavior of blood over a wide range of shear-rates, from a low of $0.06\,s^{-1}$ to as high as $650\,s^{-1}$. The model equations, however, presented the problem of infinite viscosity being recorded at zero shear-rate. To correct this anomaly, a low shear-rate criterion was implemented to ensure a finite viscosity at zero shear-rate and also to capture viscosity variations in the low shear-rate range, $0\,s^{-1}$ to $0.06\,s^{-1}$. Recent numerical tests have shown that the low shear-rate criterion [32, 33, 34, 35, 36] is not suitable for numerical implementation in complex geometries such as those used in this thesis. The reasons for this are primarily that the criterion does not allow for convergence of the residuals of the numerical equations, specifically the resultant numerical oscillations which would not die out under the conditions of the criterion. For these reasons, developed an alternate low shear-rate criterion which would ensure smooth transitions through the cut-off shear-rate of $0.06\,s^{-1}$, as well also ensuring a finite apparent viscosity at zero shear-rate.

The polymer stress for the Generalized Oldroyd-B model satisfies the same nonlinear constitutive equation as the usual Oldroyd-B model, Eq. (1.8), except the polymer viscosity is now shear-rate dependent, see Eq. (1.13),

$$\boldsymbol{\tau}_p + \lambda \overset{\nabla}{\boldsymbol{\tau}}_p = 2\eta_p(\dot{\gamma})\, \boldsymbol{S}. \tag{1.13}$$

1.4.4 Giesekus model

The shear-thinning Giesekus viscoelastic constitutive model is a generalization of both the Generalized Oldroyd-B model and the Oldroyd-B model. Additionally, the Giesekus model is capable of describing shear-banding characteristics [20, 21, 38, 39] .

The shear-thinning Giesekus viscoelastic constitutive model is described mathematically by Eq. (1.15),

$$\boldsymbol{\tau}_s = 2\eta_s \boldsymbol{S}, \tag{1.14}$$

$$\boldsymbol{\tau}_p + \alpha\, (\boldsymbol{\tau}_p \cdot \boldsymbol{\tau}_p) + \lambda \overset{\nabla}{\boldsymbol{\tau}}_p = 2\eta_p(\dot{\gamma})\, \boldsymbol{S}. \tag{1.15}$$

The Giesekus nonlinear parameter, α is also referred to as the mobility factor and is associated with the anisotropic Brownian motion or anisotropic hydrodynamic drag [1, 2]. Taking $\alpha = 0$ reduces the Giesekus model reduces to the (Generalized) Oldroyd-B model. The nonlinear term $(\boldsymbol{\tau}_p \cdot \boldsymbol{\tau}_p)$ enables simple qualitative descriptions of a number of well-known properties of viscoelastic fluids, most importantly shear-banding [23]. A comprehensive survey of viscoelastic constitutive models in common use can be found in [1, 2, 23, 40].

Chapter 2

Overview of the finite volume methods

The coupled and nonlinear systems of mathematical model equations governing fluid behavior and flow cannot be solved through analytical techniques. A recourse must be made to approximate solution methods. Approximate solutions are also known as numerical solutions. Numerical analysis is the branch of mathematics that deals with the development, theoretical exposition (analysis), and implementation of numerical solution algorithms. Numerical solution techniques have been largely aided by the rapid development of powerful computers. Numerical solution methods are therefore now routinely coupled with powerful scientific computing software to tackle complex mathematical model equations of real world phenomena and of increasing sophistication. In this thesis, the efficient finite volume numerical methods for fluid dynamics are coupled to the powerful and open-source OpenFOAM software platform.

2.1 Brief history of numerical methods

Numerical algorithms are almost as old as human civilization. The Rhind Papyrus (˜1650 BC) of ancient Egypt describes a root finding method for solving a simple equation, [42]. Archimedes of Syracuse (287 - 212 BC) created the "method of exhaustion" for calculating lengths, areas, and volumes of geometric figures, [43]. This method has is in practically the spirit of modern numerical integration, indeed it could be considered an important precursor to the development of the calculus by Isaac Newton and Gottfried Leibnitz. The invention of calculus in itself served as a fundamental motivator for the development of numerical solution techniques, especially given that the advent of calculus laid the foundations for the development of complex mathematical models across the breath of the physical and natural sciences, health science, engineering, and commerce. Another important milestone in the development of numerical solution methodologies was the invention of logarithms by Napier (1614) and others, leading to much simpler ways of carrying out the arithmetic operations of multiplication, division, and exponentiation, [44].

Mathematical models for real physical problems are largely posed as differential, integral, or integro-differential equations. Fluid dynamical equations are most naturally posed as systems of coupled nonlinear Partial Differential Equations (PDEs). Various numerical methodologies have been developed over the years for obtaining approximate solutions of PDEs, these include the Finite Difference Methods (FDM), the Finite Element Methods (FEM) [50], and the Finite Volume Methods (FVM), etc.

2.2 Finite Volume Methods (FVM)

The Finite Volume Methods (FVM) are among the most versatile numerical techniques for solving fluid dynamical problems in fluid dynamics [45]. FEM are badly suited for the solution of turbulent flows and FDM suffer from lack of conservativeness which is a problem given that fluid dynamical equations are obtained via conservation laws of physics. The FVM are uniquely designed to account even for turbulent flows and hence present a natural advantage over the FEM. Also FVM are locally and globally conservative, being developed from the same conservation principles as the fluid dynamical equations. The FVM are also perfectly suited to complex geometries and hence they (FVM) are far superior to the FDM. The FVM are quite easy to implement with any of a variety of boundary conditions in a non-invasive manner, since the unknown variables are evaluated at the centroids of the volume elements, and not at the cell boundaries.

These characteristics have made the FVM extremely well-suited for the numerical simulation of fluid flow and heat/mass transfer problems. The contemporary developments in the FVM have, indeed, been intrinsically entwined with advances in Computational Fluid Dynamics (CFD). The FVM are equally capable of resolving a wide variety of complex problems that are modelled by differential equations.

In the FVM, the solution domain is subdivided into a finite number of small control volumes (CVs) by a grid which, in contrast to the FDM, defines the control volume boundaries, not the computational nodes. Surface integrals over inner CV faces cancel out, see Eq. (2.1) and Fig. 2.1.

$$\int_S f \, dS = \sum_k \int_{S_k} f \, dS_k. \tag{2.1}$$

More generally, given a flow variable $\mathbf{\Phi}$, the transport equation for property $\mathbf{\Phi}$ can be written in conservative differential form as follows,

$$\frac{\partial}{\partial t}(m\mathbf{\Phi}) + \text{div}\,(m\mathbf{\Phi}\mathbf{u}) = \text{div}\,(\Gamma\nabla\mathbf{\Phi}) + \boldsymbol{Q}, \tag{2.2}$$

m is either the density ρ; specific heat capacity $c_v,\ c_p$; or relaxation time λ; depending on the conservation or constitutive equation and $\boldsymbol{Q}$ represents source terms. Γ is a diffusion coefficient.

Finite Difference Methods (FDM) are based on a discretization of the differential form, Eq. (2.2), of the conservation equations. FVM and FEM are based on a discretization of the integral forms of the conservation equations.

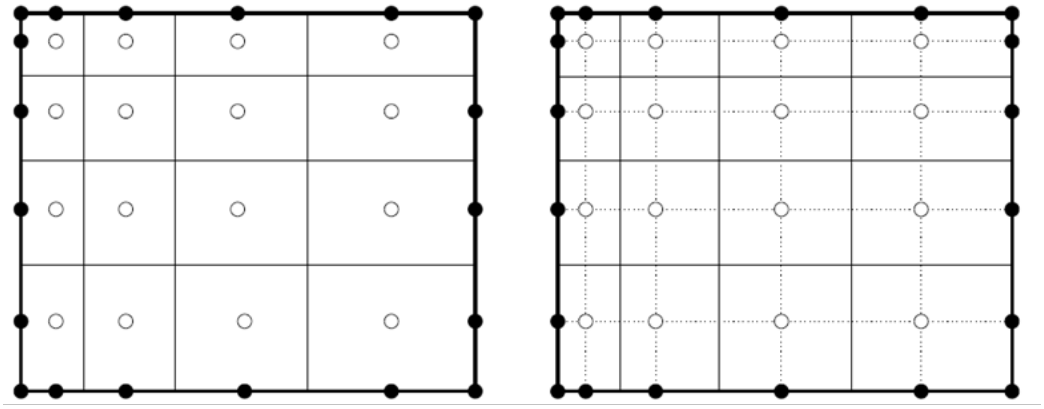

Figure 2.1: The net flux through the CV boundary is the sum of integrals over the four (in 2D) or six (in 3D) CV faces.

Figs. 2.2 and 2.3 illustrate the typical control volumes (CVs) and the notation used for the 2D and 3D Cartesian grids.

FVM are based on applying conservation principles over each small control volume Ω. In addition to local conservation, global conservation is therefore also ensured. Detailed descriptions of the FVM can be found in [45], we summarize the salient points below.

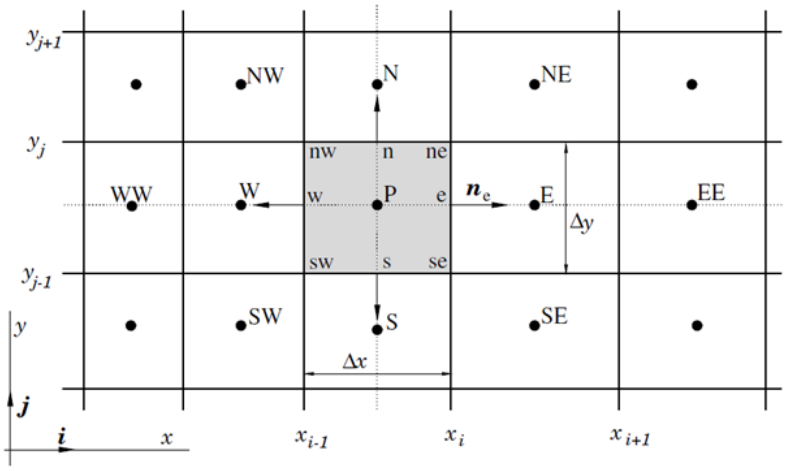

Figure 2.2: Typical CV and the notation used for a Cartesian 2D grid.

The transport equations are given in integral form: Eqs. (2.3 - 2.4) and are discretized over each control volume,

$$\frac{\partial}{\partial t}\int_\Omega m\mathbf{\Phi}\,dV + \int_\Omega \text{div}\,(m\mathbf{\Phi}\mathbf{u})\,dV = \int_\Omega \text{div}\,(\Gamma\nabla\mathbf{\Phi})\,dV + \int_\Omega \boldsymbol{Q}\,dV, \tag{2.3}$$

$$\frac{\partial}{\partial t}\int_\Omega m\mathbf{\Phi}\,dV + \int_{\partial\Omega} (m\mathbf{\Phi}\mathbf{u})\cdot\mathbf{n}\,dS = \int_{\partial\Omega} (\Gamma\nabla\mathbf{\Phi})\cdot\mathbf{n}\,dS + \int_\Omega \boldsymbol{Q}\,dV. \tag{2.4}$$

We have applied the Divergence theorem to obtain surface from volume integrals with $\mathbf{n}$ the unit normal to $\partial\Omega$.

To integrate the discrete control volume equations (2.4), we need,

- time marching methods to integrate the transient term,
- consistent methods to evaluate the fluxes at the boundary of the control volume,
- appropriate methods to evaluate the volume integrals for the source terms.

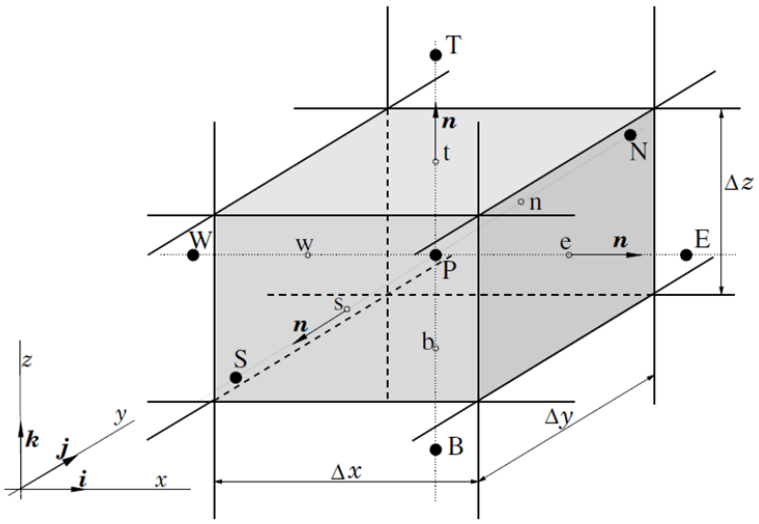

Figure 2.3: A typical CV and the notation used for a Cartesian 3D grid.

2.2.1 Time marching

If we write $\mathbf{\Phi} \leftarrow m\mathbf{\Phi}$, then the transient term reads,

$$\frac{\partial}{\partial t} \int_{\Omega} \mathbf{\Phi} \, dV.$$

If $\bar{\mathbf{\Phi}}$ is the mean value of $\mathbf{\Phi}$ within the control volume Ω (say, the value of $\mathbf{\Phi}$ at the center of the control volume) and V is the volume of Ω then,

$$\frac{\partial}{\partial t} \int_{\Omega} \mathbf{\Phi} \, dV \approx V \frac{\partial \bar{\mathbf{\Phi}}}{\partial t}.$$

This can then be integrated by any of a variety of methods; Euler, Runge-Kutta, etc.

2.2.2 Discretization of source terms

The goal is to estimate the volume integral,

$$\int_{\Omega} \boldsymbol{Q}\, dV.$$

As with the transient volume integral, the simplest approximation is the product of the volume V with the mean value of $\boldsymbol{Q}$ (i.e. $\bar{\boldsymbol{Q}}$ approximated, say, by the value at the center of the control volume $\boldsymbol{Q}_c$):

$$\int_{\Omega} \boldsymbol{Q}\, dV \approx \bar{\boldsymbol{Q}}\, V \approx \boldsymbol{Q}_c\, V.$$

The approximation is exact if $\boldsymbol{Q}_c$ is constant or linear within Ω. The approximation is second order accurate otherwise. Higher order approximation would require more locations than just the center [45].

2.2.3 Discretization of diffusive fluxes

The diffusion term is written as a sum over all the surface elements (k) that make up the bounding surface of a control volume,

$$\int_{\partial\Omega} (\Gamma \nabla \boldsymbol{\Phi}) \cdot \mathbf{n}\, dS = \sum_k \int_{\partial\Omega_k} (\Gamma \nabla \boldsymbol{\Phi}) \cdot \mathbf{n}_k\, dS \approx \sum_k \Delta\Omega_k\, (\Gamma \nabla \boldsymbol{\Phi})_k \cdot \mathbf{n}_k.$$

The diffusive flux vector $(\Gamma \nabla \boldsymbol{\Phi})_k$ for the control surface element $\Delta\Omega_k$ is approximated easily using the **central difference** methods in the direction "parallel" to $\mathbf{n}_k$.

The central differencing is only accurate if the line joining the centroids and the unit normal vector $\mathbf{n}_k$ are parallel. The approximation is therefore only correct if the mesh

is fully orthogonal. Generally, in unstructured meshes the lines connecting centroids are not parallel to $\mathbf{n}_k$. This is known as mesh skewness or non-orthogonality [45]. There are several flux correction methods to resolve such cases [45].

2.2.4 Discretization of convective fluxes

The convective term is similarly written as the sum,

$$\int_{\partial\Omega} (m\mathbf{\Phi}\mathbf{u}) \cdot \mathbf{n}\, dS = \sum_k \int_{\partial\Omega_k} (m\mathbf{\Phi}\mathbf{u}) \cdot \mathbf{n}_k\, dS \approx \sum_k \Delta\Omega_k \, (m\mathbf{\Phi}\mathbf{u})_k \cdot \mathbf{n}_k,$$

where $\mathbf{\Phi}_k$ is the value of $\mathbf{\Phi}$ at the centre of surface area element k. We need to employ discretization methods to generate the face centered values, $\mathbf{\Phi}_k$, which satisfy the requirements of conservativeness, boundedness and transportiveness. Inconsistent flux interpolation formulae, for example, give rise to unsuitable schemes that do not satisfy overall conservation [45].

Chapter 3

Implementation of FVM on OpenFOAM

3.1 Introduction to OpenFOAM

OpenFOAM is the free, open-source Computational Fluid Dynamics CFD software developed initially by OpenCFD Ltd in 2004. It has grown a large user base across most areas of engineering and science, from both commercial organizations and academic institutions. OpenFOAM has an extensive range of features to solve complex fluid flows problems involving chemical reactions, turbulence, heat transfer, etc. OpenFOAM is also extremely versatile and can be used to solve complex problems from solid mechanics, acoustics, and electromagnetics, etc.

The OpenFOAM software employs Finite Volume Methods as the underlying numerical methodology. Other open source software such as deal.ii employ Finite Element Methods (FEM). Commercial CFD packages such as ANSYS/Fluent, Star-CCM+, FloTHERM, and Commercial CFD add-ins embedded in existing CAD software (such as SolidWorks Flow Simulation, FloEFD) are very powerful and can

model different types of simple and complicated fluid dynamical and thermodynamical problems. The commercial CFD software usually have an advantage in that the user has a very good control on important aspects such as surface and volume mesh generation during pre-processing. However, commercial CFD packages come with huge disadvantages in that the license fees are quite costly and also that users need, not only a good CFD knowledge, but also comprehensive training in order to use the packages effectively. Many other open-source CFD solvers, such as SU2, Palabos, Fire Dynamics Simulator, and MFIX, are however no different. Given that it uses native mathematical language in its codes (for example the OpenFOAM code for the gradient operator, ∇, would simply be *grad*, etc.), OpenFOAM has therefore become by far the most widely used open-source CFD software. It is for this reason, among others, that OpenFOAM will be employed in this thesis.

OpenFOAM is specifically designed and tailor made to solve complex CFD problems in complex geometries. Given that the OpenFOAM libraries are fairly general, they can be used to solve any problem that is described by partial differential equations.

The OpenFOAM software package usually runs on Linux. For performance of simulations, installation of a Linux operating system was necessary. For this thesis, OpenFOAM was implemented on Ubuntu version 14.04.5 LTS.

It should also be noted here that OpenFOAM does not have a user interface (GUI) by default. This means that all commands must be entered via the command line. OpenFOAM is first and foremost a C++ library, used primarily to create executables, known as applications. The applications fall into two categories: solvers, that are each designed to solve a specific problem in continuum mechanics; and utilities, that are designed to perform tasks that involve data manipulation. New solvers and utilities can be created by a user with some pre-requisite knowledge of the underlying method, physics, and programming techniques involved.

OpenFOAM is supplied with pre- and post-processing environments. The interface to the pre- and post-processing are themselves OpenFOAM utilities, thereby ensuring consistent data handling across all environments. The standard structure for OpenFOAM simulations is shown in Figs. 3.1 and 3.2.

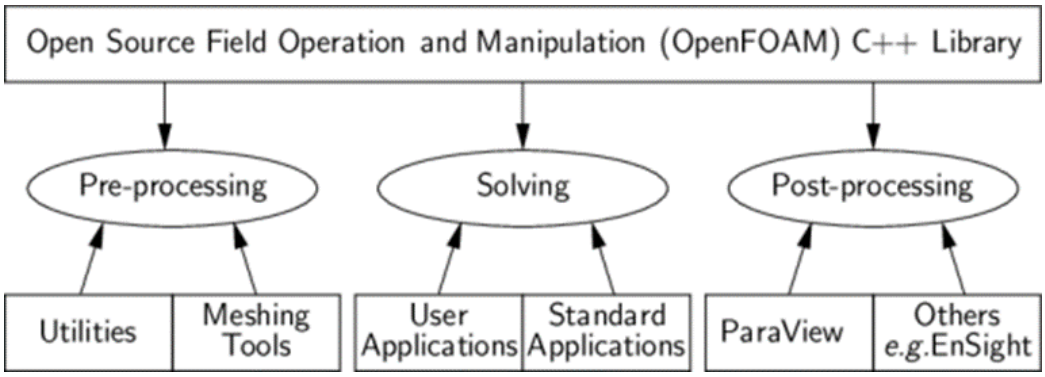

Figure 3.1: Standard structure for OpenFOAM simulations.

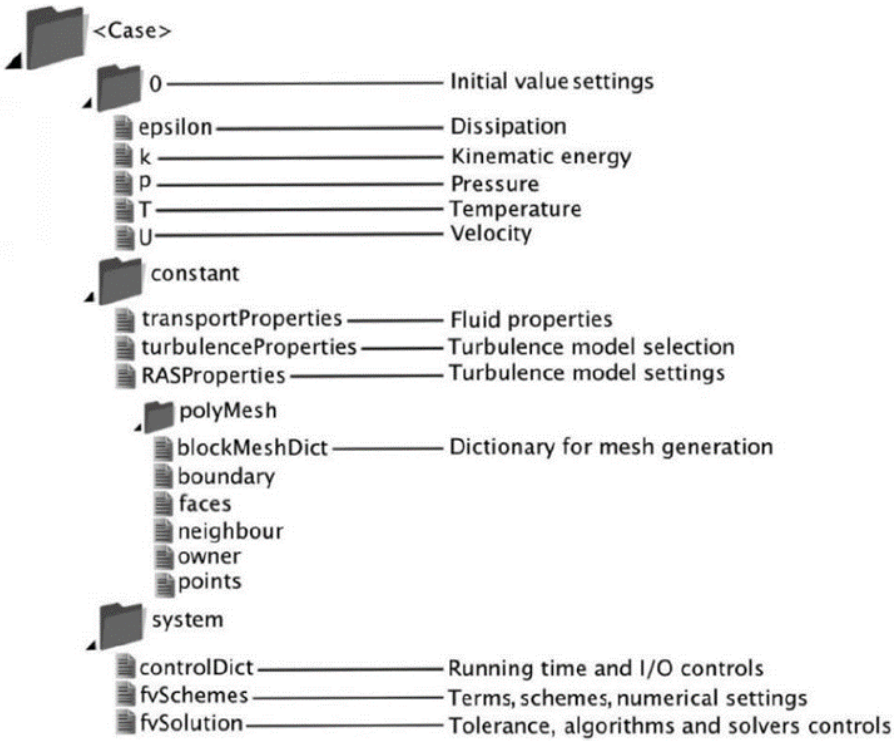

Figure 3.2: OpenFOAM Structure.

3.1.1 A constant directory

The 'constant' directory contains a full description of the case mesh in a subdirectory named *polyMesh*. The 'constant' directory also contains files specifying physical properties, say *transportProperties*, for the application under consideration.

3.1.2 A system directory

The 'system' directory is used for setting parameter values associated with the solution procedure. The directory contains at least the following 3 files: *controlDict* where run control parameters are set including start/end time, time-step and parameters for data output; *fvSchemes* where discretization schemes used in the

solution may be selected at run-time; and *fvSolution* where the equation solvers, tolerances, and other algorithm controls are set for the run.

3.1.3 The time directories

The 'time' directories contain individual files of data for particular fields. The data can be either, initial values and boundary conditions that the user must specify to define the problem or results written to file by OpenFOAM. Note that the OpenFOAM fields must always be initialised, even when the solution does not strictly require this, as in steady-state problems. The name of each time directory is based on the simulated time at which the data is written and is described fully later. It is sufficient to say now that since we usually start our simulations at time $t = 0$, the initial conditions are usually stored in a directory named 0 or 0.000000e+00, depending on the name format specified. For example, in the cavity tutorial, the velocity field $\boldsymbol{v}$ and pressure field p are initialised from files 0/U and 0/p respectively.

3.1.4 viscoelasticfluidfoam solver

The implementation of the different equations involved (continuity, momentum, and a constitutive equation) was done using the OpenFOAM C++ resources which make possible the definition of variables directly as vectors or tensors. This avoids the need of breaking the equations in all its components, through the use of a symbolic representation which is quite similar to the mathematical language. In this way, for example, the symbolic representation of Eq. (2) in OpenFOAM language is:

```
<fvVectorMatrix> UEqn
            (
              fvm::ddt(U)  + fvm::div(phi,U)  - fvc::div(tau)
            );
```

where,

$$\text{phi} = S_f \cdot (\rho \boldsymbol{v})_f$$

$S_f is the cell face surface$

fvm$is the finite volume method class used for implicit operations$

fvc$is finite volume calculus class used for explicit operations$

The terms of the equation for velocity ($\boldsymbol{v}$) are stored in a matrix that contains the equations for the three components of the vector $\boldsymbol{v}$ (*fvVectorMatrix*) named *UEqn* and this equation is solved with the command,

```
solve(UEqn() == -fvc::grad(p));
```

in which the pressure gradient is included to complete the equation. The inclusion of the pressure gradient only in this last command and not in the definition of the UEqn matrix is due to the use of the SIMPLE or PISO algorithms.

Regarding the implementation of the constitutive equations for polymeric stress tensor, the description is illustrated using the implementation of Giesekus model as an example. Table 3.1 explains how each term in the Giesekus equation is defined in foam-extend.

Table 3.1: OpenFOAM implementation of the Giesekus constitutive model

Mathematical Operator	OpenFOAM implementation
$\frac{D\boldsymbol{\tau}}{Dt}$	fvm::dt(tau_-)+fvm::div(phi( ),tau_)
$2\eta_s \boldsymbol{S}$	etaP_*twoD
$\boldsymbol{\tau} \cdot \nabla \boldsymbol{v} + (\nabla \boldsymbol{v})^T \cdot \boldsymbol{\tau}$	twoSymm(c)
$\frac{\alpha}{\eta_p}(\boldsymbol{\tau} \cdot \boldsymbol{\tau})$	(alpha_/etaP_) *symm(tau_-&tau_-)
$\frac{1}{\lambda}\boldsymbol{\tau}$	fvm::Sp(1/lambda_,tau_)

Table 3.1 especially illustrates the efficiency of the OpenFOAM software platform in allowing the mathematical equations to be described in their native form, rather than in the discretized form, as with the FDM, or in the weak form as in the FEM.

3.1.5 Numerical flow algorithm

A summary flow diagram of the numerical algorithm implementation in OpenFOAM is given in Fig. 3.3.

The numerical algorithms as developed in this thesis are designed to be general-purpose to fit a broad range of viscoelastic constitutive models of the Oldroyd-B type. These numerical algorithms are implemented on the OpenFOAM software and, in the next chapter, are validated against existing benchmark flow problems in the literature.

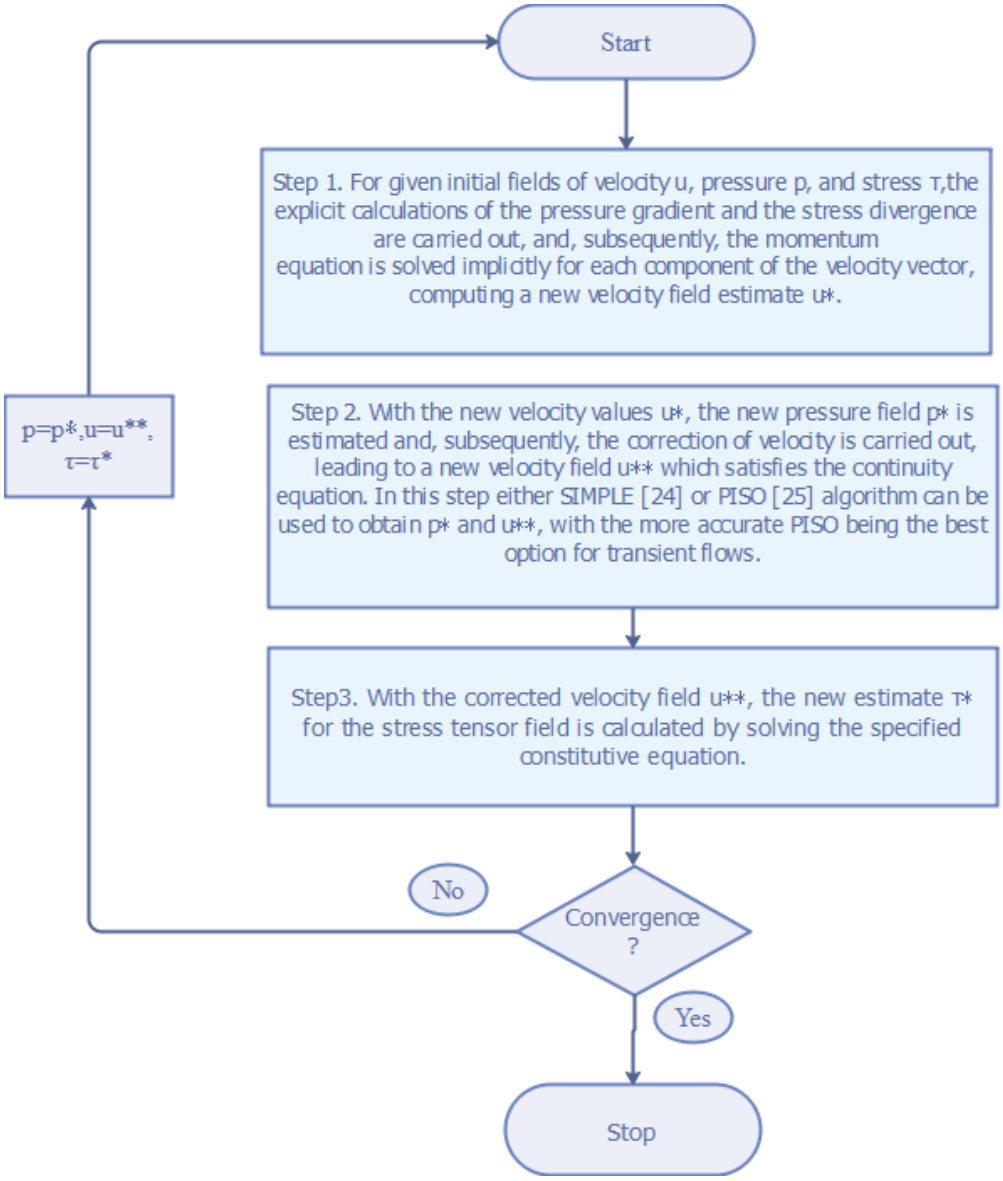

Figure 3.3: Numerical Flow Algorithm.

Chapter 4

Code validation

The 4:1 contraction flow problem represents perhaps the most widely used standard benchmark problem for viscoelastic fluid flow computations. The 4:1 contraction flow geometry will be used as the benchmark case to validate the utility and robustness of the numerical algorithms developed in this thesis.

Noting that the Giesekus viscoelastic constitutive model is a generalization of both the Oldroyd-B and Generalized Oldroyd-B models, the validation exercise will also naturally be conducted via the Giesekus model. This allows for the development of a general purpose code for fluids described by any of these three viscoelastic constitutive models.

Fig. 4.1 gives an illustration of the typical 4:1 contraction geometry that will be used to benchmark the numerical algorithms developed in this thesis. The entry flow configuration is standard, as shown in Fig. 4.1. The ratio of the upstream thickness H to the downstream thickness h is $H/h = 4$, hence the term 4:1 contraction. An orthogonal Cartesian coordinate system is adopted, with the z-axis in the streamwise direction and x- in the transverse direction.

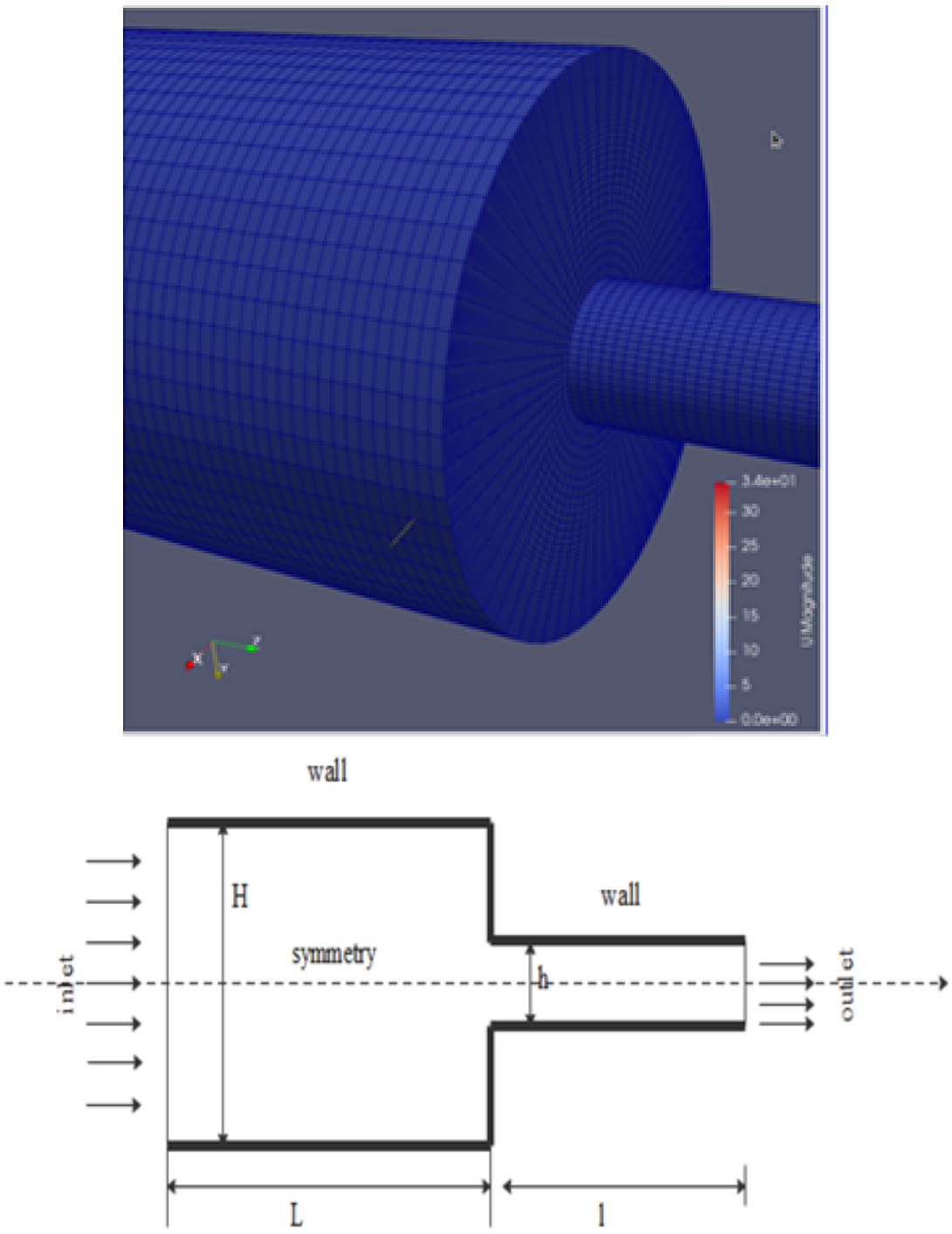

Figure 4.1: Geometry of the 4:1 contraction flow problem.

4.1 Initial and boundary conditions

Table 4.2 gives a list of the initial values for the 4:1 contraction flow problem using the Giesekus model.

Table 4.1: Initial flow conditions for Giesekus model

Variable	Initial value
Velocity	$1.55\,\mathrm{m/s}$
Density	$803.87\,\mathrm{kg/m^3}$
Solvent viscosity	$0.002\,\mathrm{kg\,m^{-1}\,s^{-1}}$
Polymer viscosity	$1.422\,\mathrm{kg\,m^{-1}\,s^{-1}}$
Relaxation time	$0.003\,\mathrm{s}$
Reynolds Number	3.49

The following boundary conditions are implemented.

- Wall boundary conditions: the no-slip conditions for the velocity are employed.
- Channel centerline: the symmetry condition for the velocity is enforced.
- Channel inlet: the velocity value is obtained by dividing the prescribed downstream average velocity by four and the stress tensor is considered null.
- Channel outlet: the velocity gradient along the x-direction, as with the pressure, are taken as zero. The zero-gradient boundary condition is used for the polymer stresses.

4.2 Mesh generation

The flow geometry and its corresponding meshing are generated via OpenFOAM's *blockMeshdict* and *blockMesh* utilities, see Fig. 4.2.

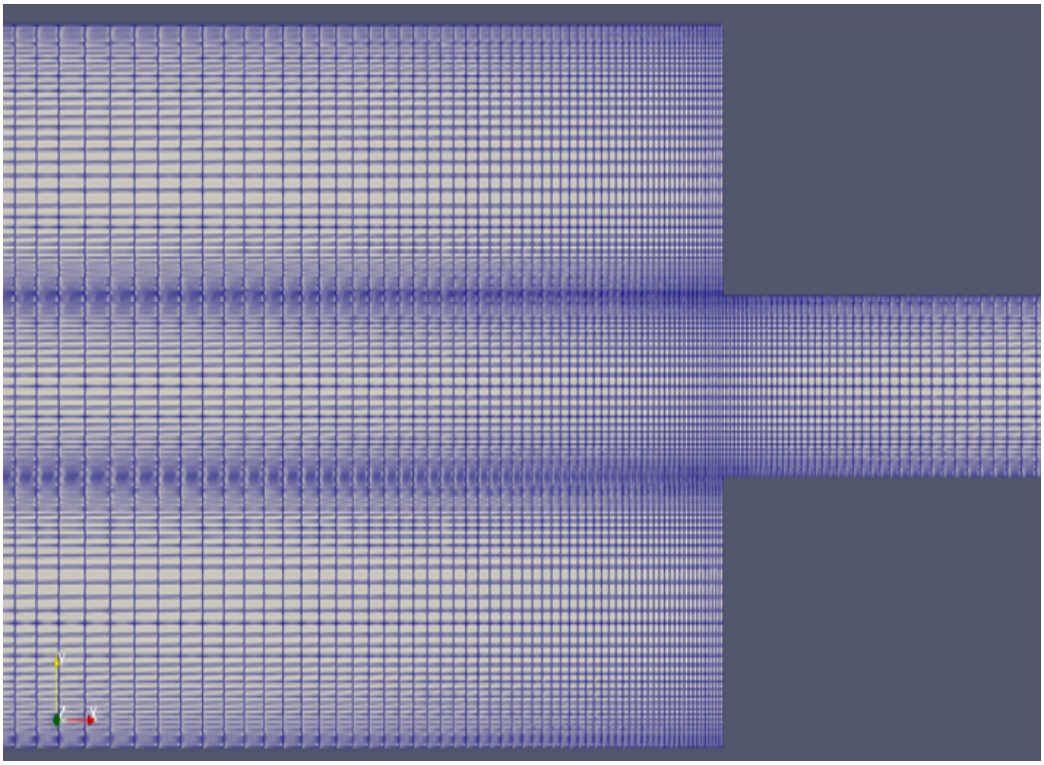

Figure 4.2: Mesh generation via blockMesh.

Two types of mesh (depicted Mesh 1 and Mesh 2) are employed for comparative purposes, see Table 4.2. Much smaller elements are generally required around the contraction region to account for the dramatic stress effects (specifically the first normal stress difference effects) that develop in the vicinity of the contraction. Table 4.2 gives the number of elements, the total number of nodes, as well as the area of the element adjacent to the contraction region for each grid.

Table 4.2: Meshing Characteristics

	Mesh 1	Mesh 2
Number of Cells	659200	673400
Number of Nodal points	673599	686463

4.3 Benchmark results

The main aim of numerical simulations is to approximate the behavior of physical systems on a computer to a high degree of precision. Numerical and computational simulations are now quite well-established and indeed routinely used to complement experimental methodology in many applications from the fields of solid mechanics, fluid mechanics, thermodynamics, acoustics, etc. Numerical and computational simulations play a crucial part in the designing phase of product development, where numerical simulations are carried out in advance of virtual prototyping, prior testing, and optimization for time and cost efficiency. The range of application of numerical simulation continues to grow exponentially, including in stress–strain simulations to estimate the crash worthiness of automobile parts; stress analyses of high-speed helical gears to reduce failures; optimal design, accurate prediction of flight vehicle characteristics for commercial aeroplanes; etc. [46, 47, 48, 49].

CFD problems often lead to large systems of equations that are computationally too expensive to solve on classical computers. Model order reduction methods aim to solve this problem by decreasing the complexity and computational cost of a system by removing "redundant" information from the models. The main idea is to generate computationally efficient methods that work with a relatively high accuracy at points of interest and to remove any unnecessary complications in the model otherwise. One example is the Proper Orthogonal Decomposition (POD) method, which is a widely used snapshot-based reduction method for CFD applications.

To test the influence of mesh refinement on the convergence of the simulations, we plot profiles of the first normal stress difference (N_1) in the vicinity of the contraction. The most challenging conditions of convergence are indeed expected in the vicinity of the contraction. The graphical results demonstrate that the coarser grid, Mesh1,

equally leads to good convergence of solutions and hence the subsequent simulations will be limited to this coarser grid choice to reduce computational costs.

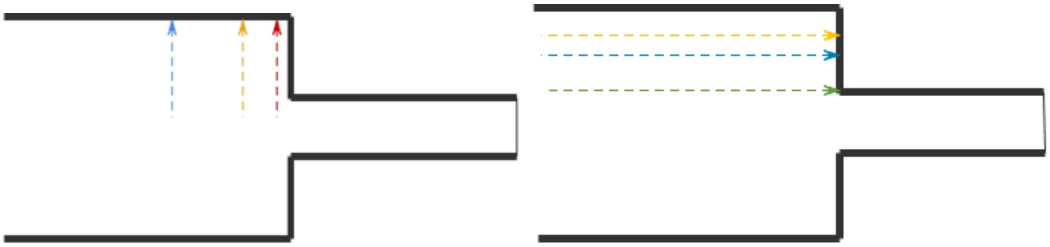

Figure 4.3: Transverse and longitudinal positions for benchmark velocity profiles.

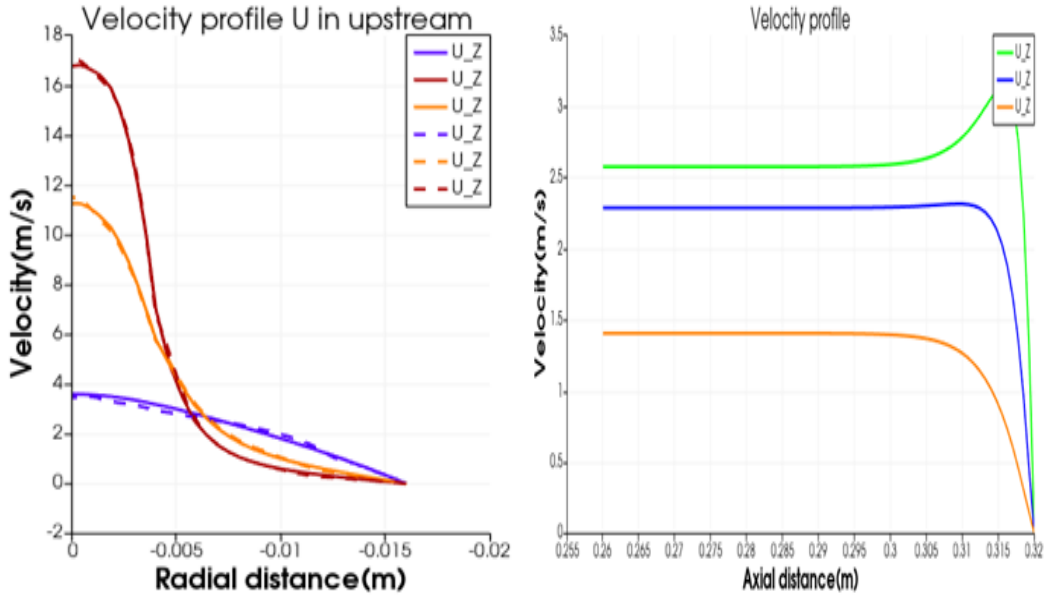

Figure 4.4: Benchmark results for transverse and longitudinal velocity.

The results for the longitudinal-velocity Fig. 4.4 (RHS) show, as expected that the velocity closer to the channel centerline would be correspondingly higher than that closer to the channel walls. Given the no-slip and impermeability boundary conditions at solid walls, the drop in velocity to zero in the vicinity of the contraction is to be expected. Indeed, Fig. 4.3 shows that the longitudinal positions at which the

longitudinal-velocity is plotted all end up at the impermeable vertical contraction-wall at which the longitudinal-velocity would abruptly drop to zero, naturally!

The transverse-velocity results are illustrated in Fig. 4.4 (LHS). The transverse-velocity is highest in the vicinity of the vertical contraction-wall given the need for the fluid to "turn" from its longitudinal trajectory, negotiate the contraction corners in the transverse direction, and flow towards the narrower contraction section leading to the outlet. As one moves farther away from the vertical contraction-wall in the left hand direction towards the channel inlet, the fluid's need to turn and change direction correspondingly diminishes (given that there are no obstacles, corners, forcing such directional changes) and hence the transverse velocity components correspondingly diminish in this direction as illustrated in Fig. 4.4 (LHS).

The solid-line graphs in Fig. 4.4 (LHS) represent the finer mesh and the dashes-line graphs are results obtained from the coarser mesh. Both mesh choices give similar solutions and hence in subsequent sections, attention will be limited to the coarser mesh given the need to minimize computational costs.

Figs. 4.5 & 4.6 for the shear stress, τ_{12}, results and Figs. 4.7 & 4.8 for the first normal stress difference, $N_1 = \tau_{11} - \tau_{22}$, results; are analogous to Figs. 4.3 & 4.4 and plotted at different transverse and longitudinal channel positions. Dramatic behaviour of the polymer stresses is observed in the vicinity of the contractions. Specifically, spikes in the strengths of the polymer stresses are observed.

Figs. 4.9 & 4.10 for longitudinal τ_{12} and N_1 profiles allowing for the fluid to move downstream the contraction towards the outlet. We notice, as expected, a spike in the polymer stresses in the vicinity of the contraction. Once the fluid has negotiated the contraction, the stresses reduce to "normal" levels downstream of the contraction. These results explain the dramatic behaviour observed in flow of viscoelastic fluids in

contraction geometries, especially in the vicinity of the contractions, see for example [38, 39].

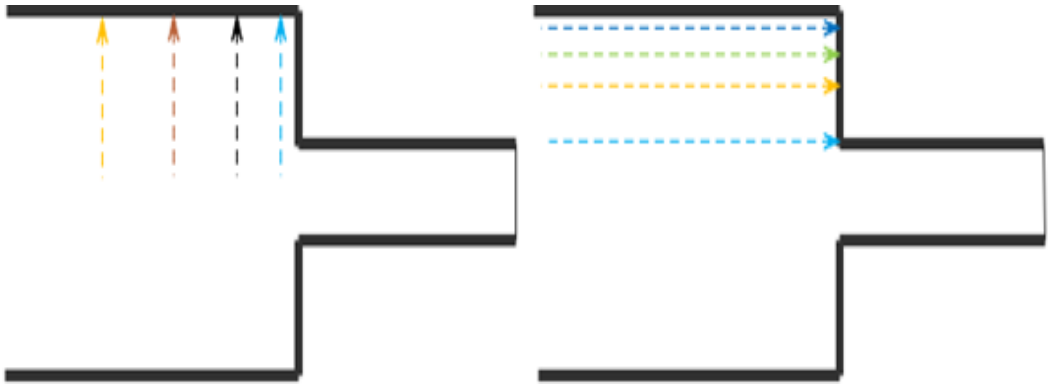

Figure 4.5: Transverse and longitudinal positions for benchmark τ_{12} profiles.

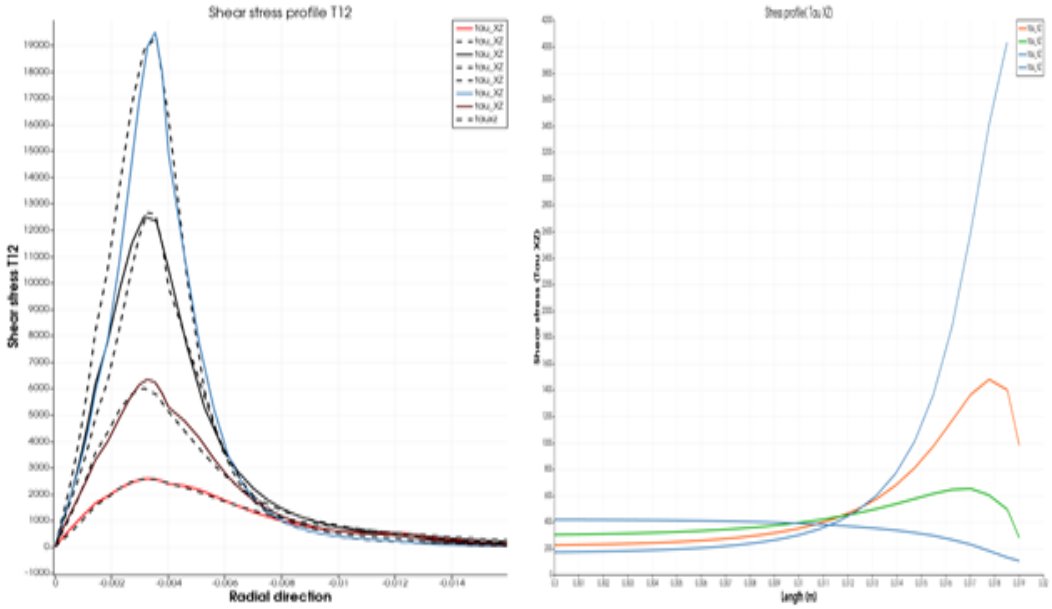

Figure 4.6: Benchmark results for transverse and longitudinal stress, τ_{12}.

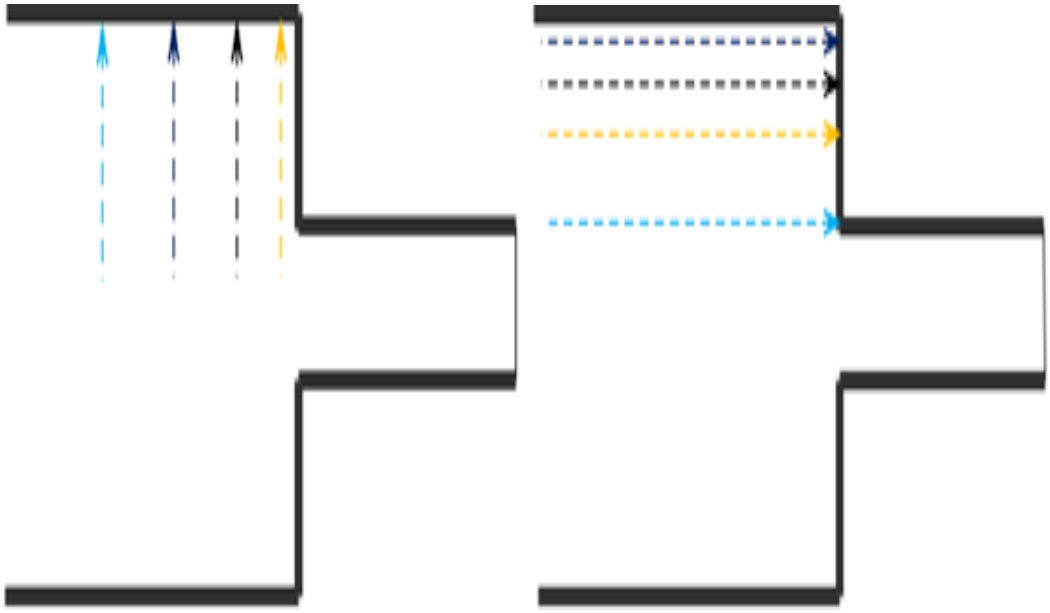

Figure 4.7: Transverse and longitudinal positions for benchmark N_1 profiles.

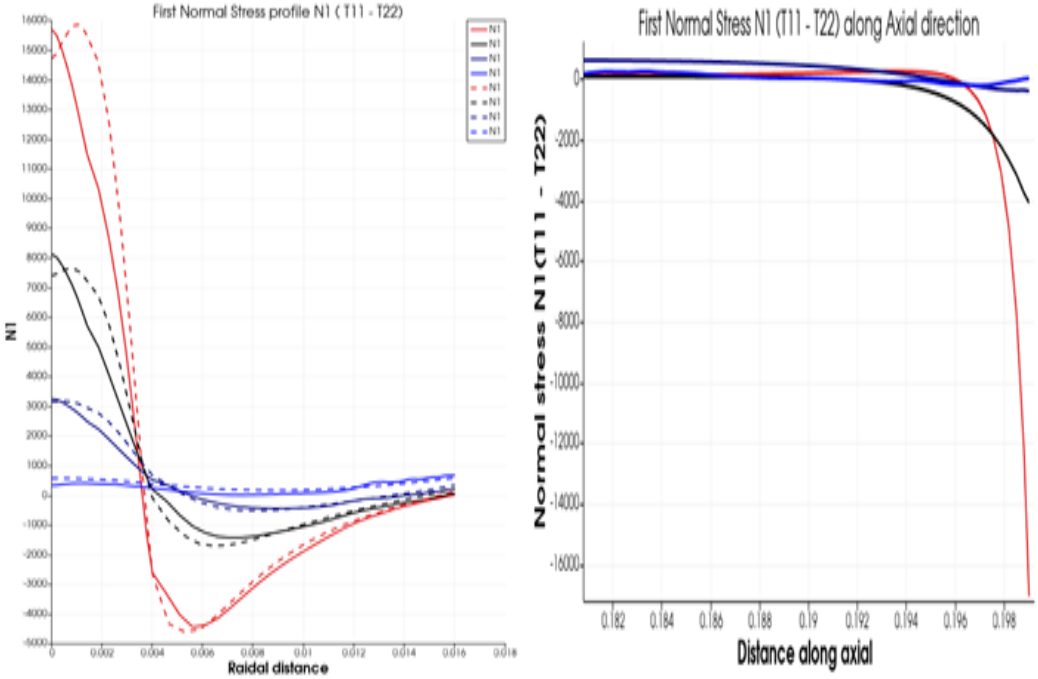

Figure 4.8: Benchmark results for transverse and longitudinal N_1.

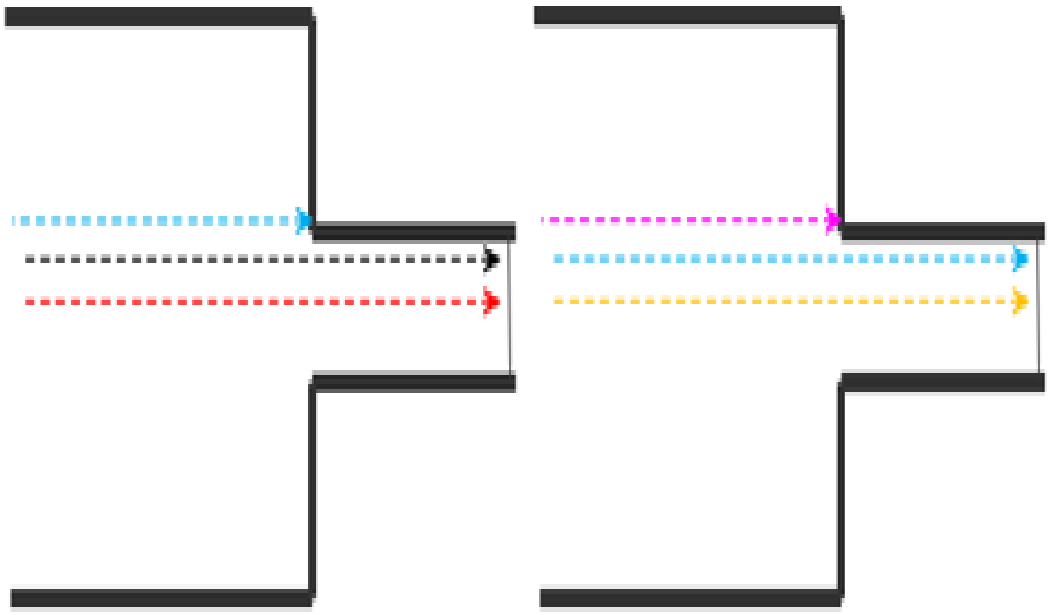

Figure 4.9: Transverse and longitudinal positions for benchmark τ_{12} and N_1 profiles.

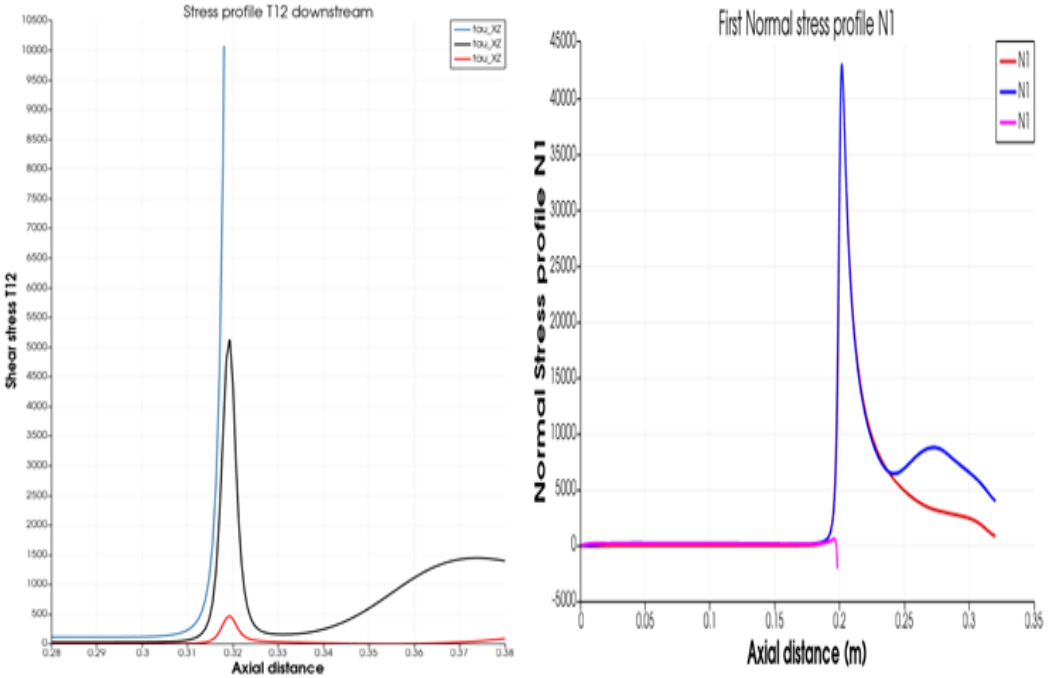

Figure 4.10: Benchmark results for transverse and longitudinal τ_{12} and N_1.

4.4 Numerical validation with Oldroyd-B results

Velocity contour plots and streamlines in a 4:1 contraction channel for using the Oldroyd-B model were obtained in [51]. Figs. 4.11 through 4.13 show the comparison of the results from our computations against the published results in [51].

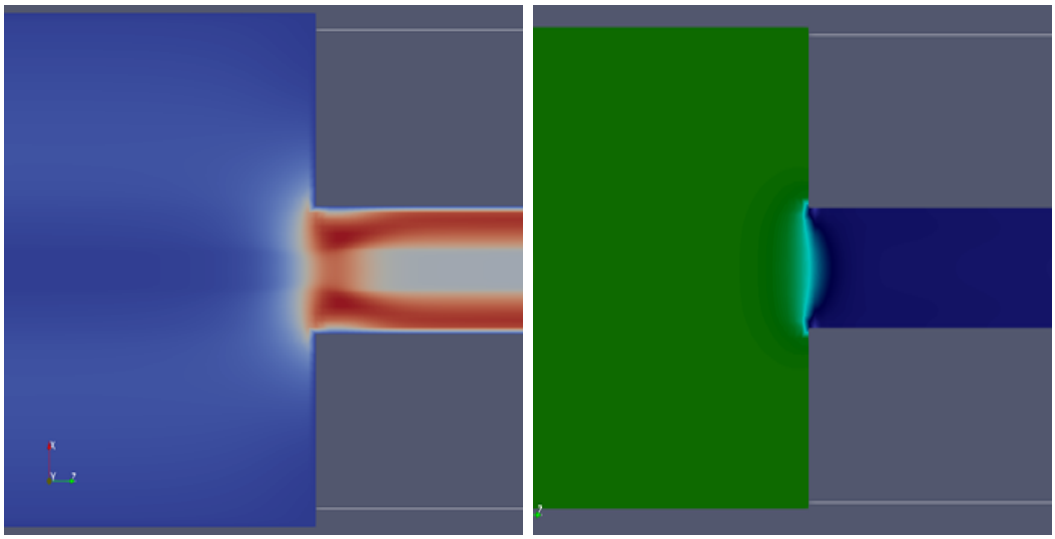

Figure 4.11: Oldroyd-B benchmark velocity results; this work (LHS) vs. [51] (RHS)

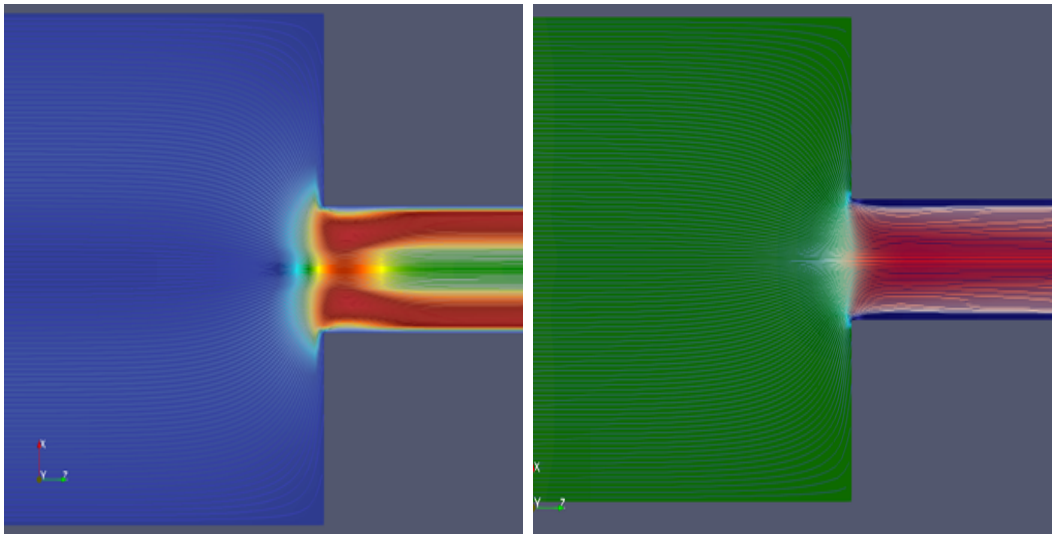

Figure 4.12: Oldroyd-B benchmark velocity results; this work (LHS) vs. [51] (RHS)

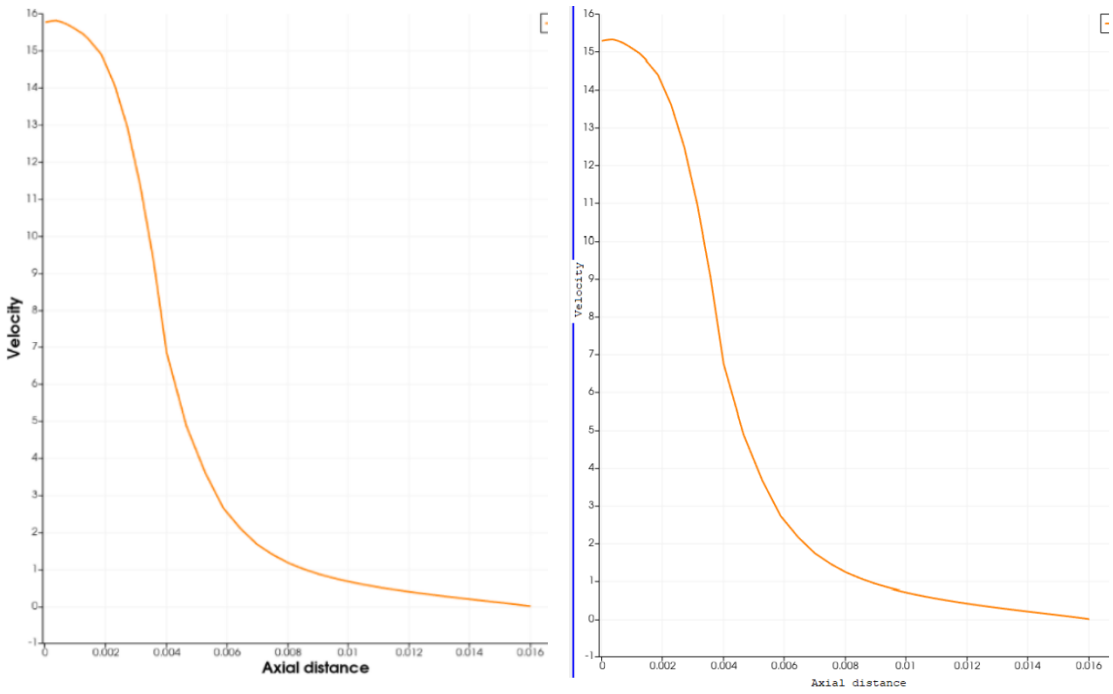

Figure 4.13: Oldroyd-B benchmark velocity results; this work (LHS) vs. [51] (RHS)

In all cases illustrated in Figs. 4.11-4.13, excellent qualitative and quantitative agreement with the numerical results of [51] is observed. The numerical schemes and meshes used in [51] are not the same as those used in the present work and hence the results give excellent validation to the robustness of the numerical algorithms developed in this thesis.

4.5 Novel Generalized Oldroyd-B results

Fig. 4.14 presents new results for the Generalized Oldroyd-B viscoelastic constitutive model. For ease of reference and for consistency, the parameters used to produce the results of Fig. 4.14 are otherwise the same as those for Figs. 4.11-4.13, save for the inclusion of shear-rate dependent viscosity in Fig. 4.14. The shear-viscosity for the normal Oldroyd-B fluid (from Figs. 4.11-4.13) stays constant throughout the channel,

from the inlet to the outlet. However, the decrease in shear-rates as one moves from the inlet towards the contraction means that the shear-viscosity for the Generalized Oldroyd-B fluid would correspondingly decrease. This explains the correspondingly lower velocities for the Generalized Oldroyd-B fluid, Fig. 4.14, compared to the velocities for the Oldroyd-B fluid, Figs. 4.11-4.13.

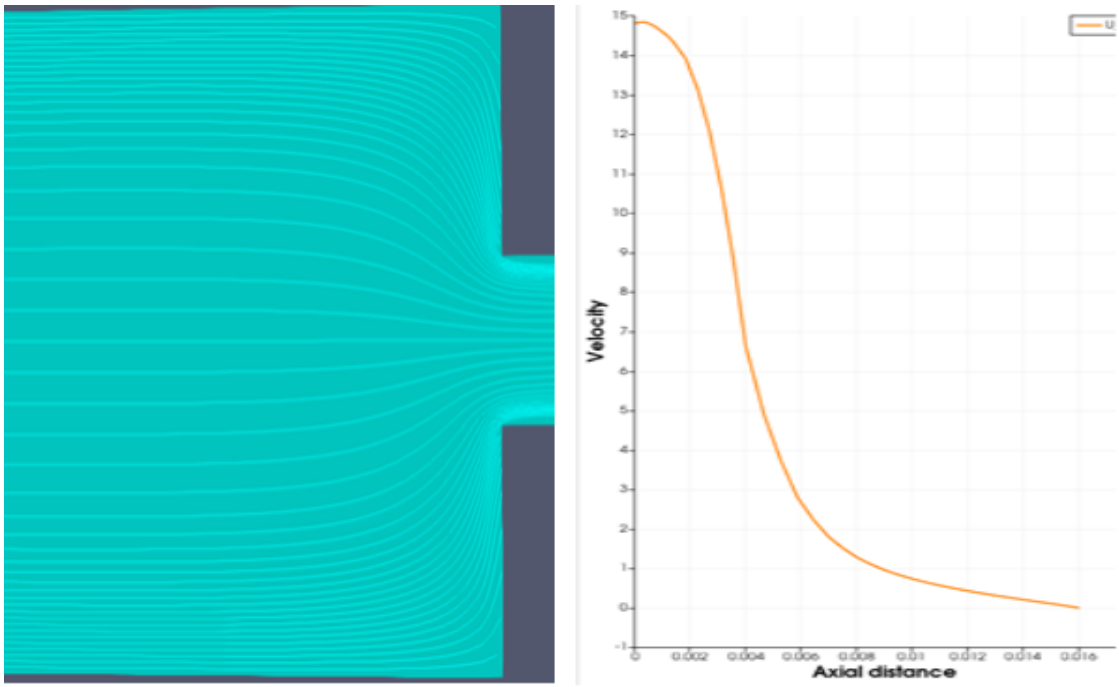

Figure 4.14: Novel Generalized Oldroyd-B velocity results.

We have demonstrated that the general-purpose code developed in this thesis performs extremely well as validated against benchmark result for the quite general Giesekus viscoelastic constitutive model. The Giesekus model encompasses the Oldroyd-B type models and hence the general-purpose nature of the numerical algorithms based on the Giesekus model. In the following chapters, we focus on the blood flow modelling, in stenosed and bifurcating arteries, via the Oldroyd-B and Generalized Oldroyd-B models which represent the most widely accepted constitutive models for blood.

Chapter 5

Oldroyd-B modelling of blood flow in stenosed and bifurcating arteries

Heart diseases and related ailments linked to the blood circulatory system are a leading cause of death [7, 52, 53, 54, 55]. It is therefore important to understand the blood flow behaviour and characteristic in blood vessels, such as arteries. A considerable number of theoretical and experimental studies have therefore been conducted on blood flow through, say, the arterial system [9, 13]. The blood flow characteristics in the arteries strongly depend on the fluid-dynamical attributes of blood, such as viscosity, pressure, concentration, turbulence, etc. The deposit and accumulation of fatty material along the inner linings of arteries lead to the development of arterial stenosis which would obstruct the normal flow of blood and hence also the supply of nutrients and antibodies to different parts of the body. Given the need for distribution of blood and its constituents to vast areas in the entire body, the blood vessels must of necessity branch out (bifurcate) in order to reach all such areas. We are specifically interested in investigating the effects of such an arterial bifurcation in the vicinity of an arterial stenosis.

The influence of time dependent development of arterial-like stenosis using Newtonian fluids flowing through an axially symmetric tube was investigated in [56]. The work in [52] studied the pulsatile flow of blood in a distensible aortic bifurcation subject to the body acceleration and observed that the flow patterns in the parent aorta were not interrupted by the body acceleration and the wall distensibility, but there is a profound change in the daughter artery. Investigations in [53] reported that wall shear-stress measurements may be used for the assessment of strength of the affected wall of the blood vessel. The time variant response of non-Newtonian blood flow through a stenosed artery in the presence of a magnetic field is explored in [28]. The work of [54] examined the effect of stenosis on non-Newtonian flow of blood in constricted blood vessel and concluded that the height of the stenosis has a direct relation with shear-stress and impedance while reversal relationship vary with flow-rate. The clear conclusion that the flow patterns are strongly related to the geometry of artery and stenosis was demonstrated in [55].

In the present chapter, an Oldroyd-B model of blood is adopted to investigate the blood flow characteristics in a stenosed and bifurcating artery. The Oldroyd-B model for blood would account for the elastic behaviour of blood, which is otherwise missed by the investigations cited above. The subsequent chapter extends this work to Generalized Oldroyd-B models for blood in order to additionally account for shear-dependent viscosity.

5.1 Flow geometry

Fig. 5.1 gives a schematic illustration of the model problem. We consider an artery of normal diameter D which bifurcates into two daughter arteries, each of diameter $D/2$. A symmetric stenosis, of length L, exists along a potion of the parent artery

on the left hand side of the symmetric bifurcation. We assume that the stenosis reduces the diameter of the artery, at stenosis, by 50%, 70%, or 90% respectively and thereby analyze the corresponding changes in velocity, pressure, and shear-stress. A rectangular cartesian coordinate system is adopted, with the x-axis in the stream-wise direction and the y-axis oriented in the transverse direction.

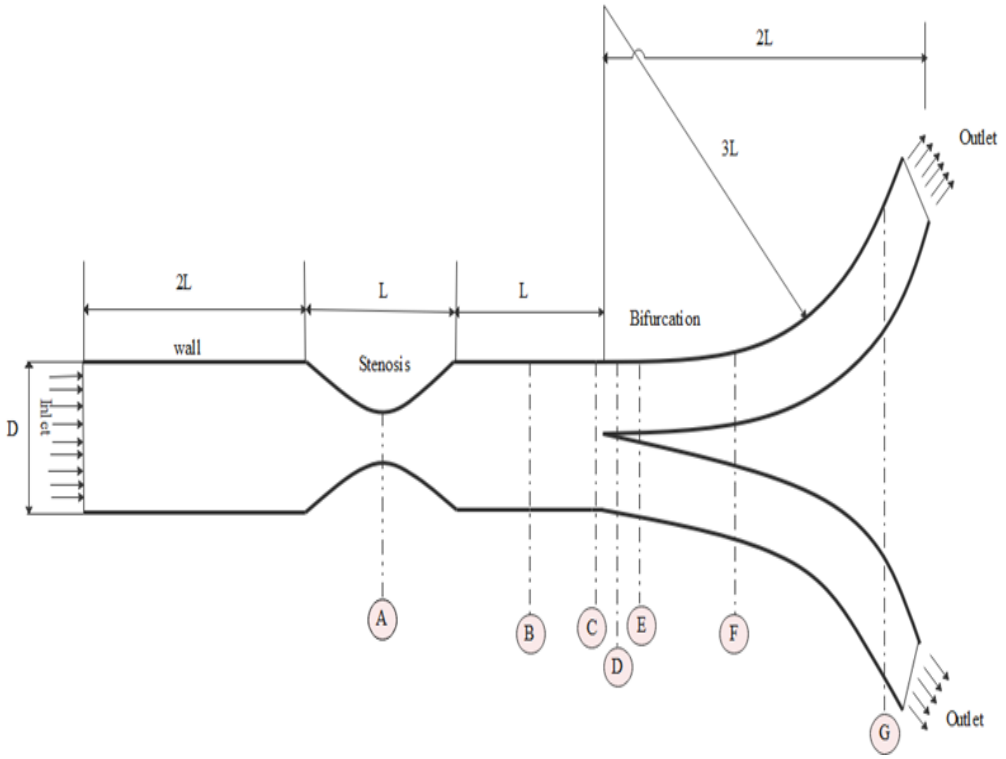

Figure 5.1: Schematic of the arterial geometry showing a symmetric stenosis and bifurcation.

5.2 Flow assumptions

In Fig. 5.1, it is implicitly assumed that the blood flow is steady, laminar, incompressible, isothermal, and of homogeneous concentration. Table 5.1 gives a list of the initial values for the blood flow problem.

Table 5.1: Initial flow conditions for Oldroyd-B model

Variable	Initial value
Velocity	$0.33\,\mathrm{m/s}$
Density	$1050.87\,\mathrm{kg/m^3}$
Solvent viscosity	$0.0067\,\mathrm{kg\,m^{-1}\,s^{-1}}$
Polymer viscosity	$0.0017\,\mathrm{kg\,m^{-1}\,s^{-1}}$
Relaxation time	$0.008\,\mathrm{s}$
Reynolds Number	82.5

The following boundary conditions are implemented.

- Wall boundary conditions: the no-slip conditions for the velocity are employed.
- Channel centerline: the symmetry condition for the velocity is enforced.
- Channel inlet: the velocity value is obtained by dividing the prescribed downstream average velocity by four and the stress tensor is considered null.
- Channel outlet: the velocity gradient along the x-direction, as with the pressure, are taken as zero. The zero-gradient boundary condition is used for the polymer stresses.

5.3 Mesh generation

The flow geometry and its corresponding meshing are generated via OpenFOAM's blockMeshdict and blockMesh utilities, see Fig. 5.2.

The specific mesh characteristics for each respective scenario corresponding to 50%, 70%, or 90% blockage respectively are illustrated in Figs. 5.3, 5.4, and 5.5.

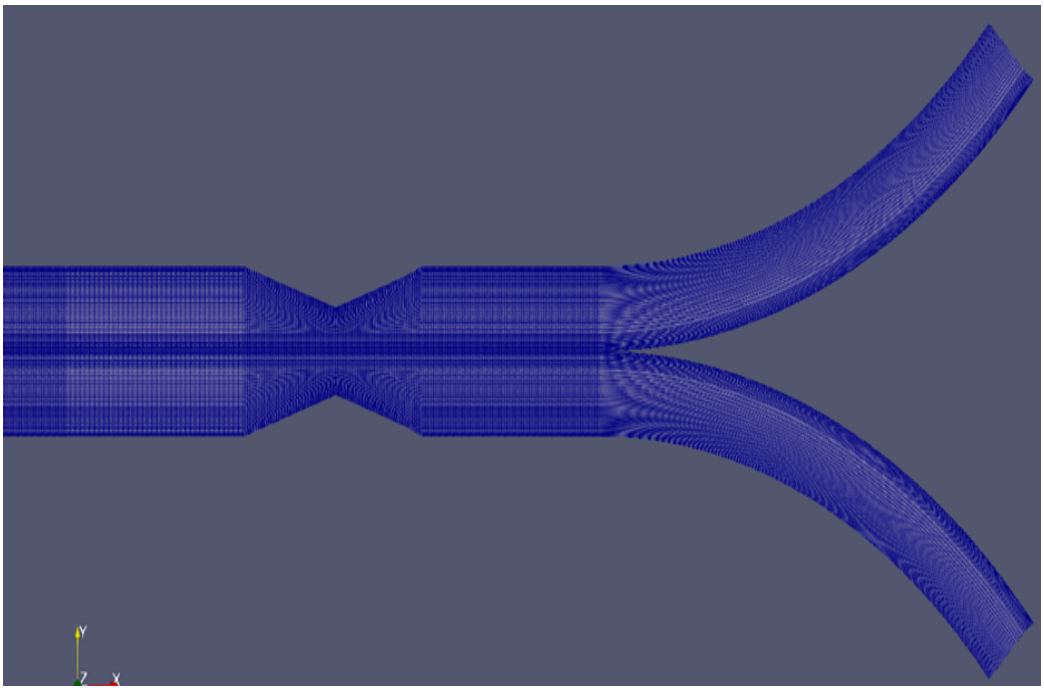

Figure 5.2: Mesh generation via blockMesh.

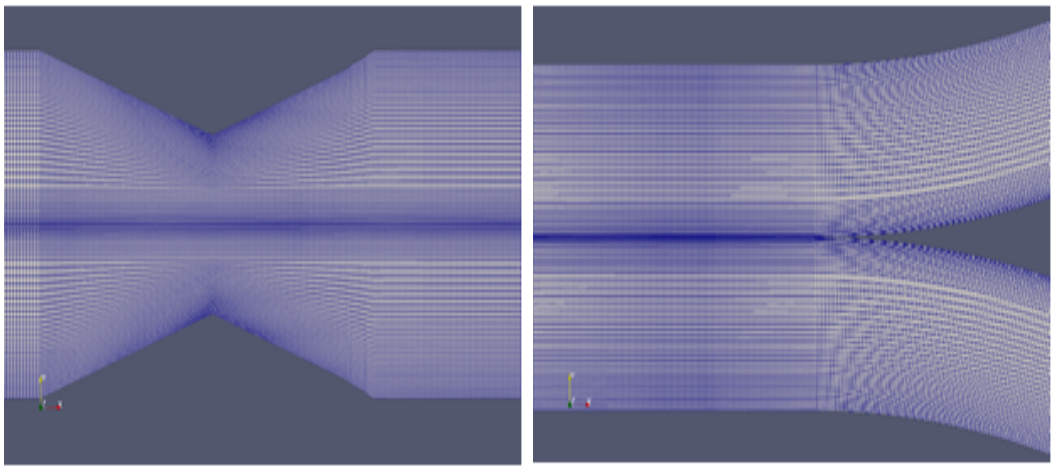

Figure 5.3: Case 1, 50% blockage, 76,500 cells, 155,482 nodal points.

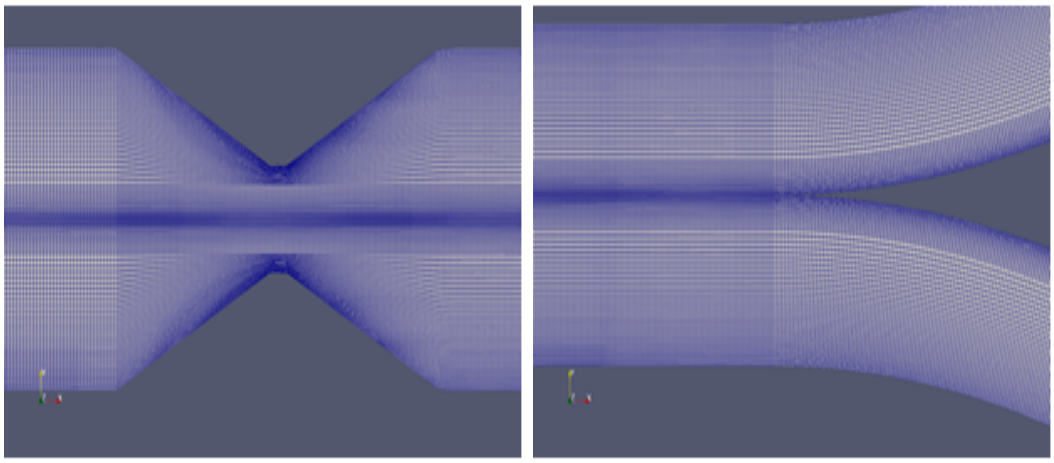

Figure 5.4: Case 2, 70% blockage, 102,000 cells, 206,542 nodal points.

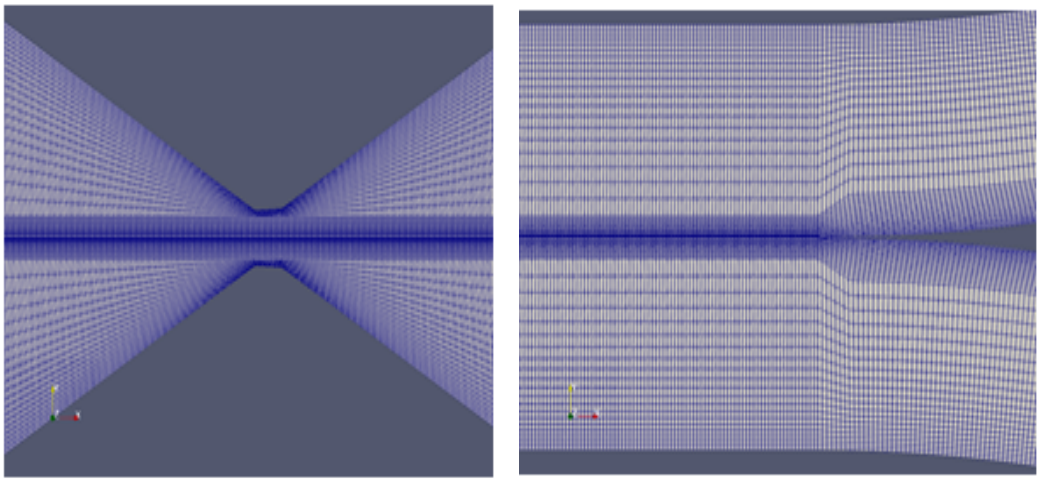

Figure 5.5: Case 3, 90% blockage, 76,000 cells, 154,662 nodal points.

5.4 Oldroyd-B Results

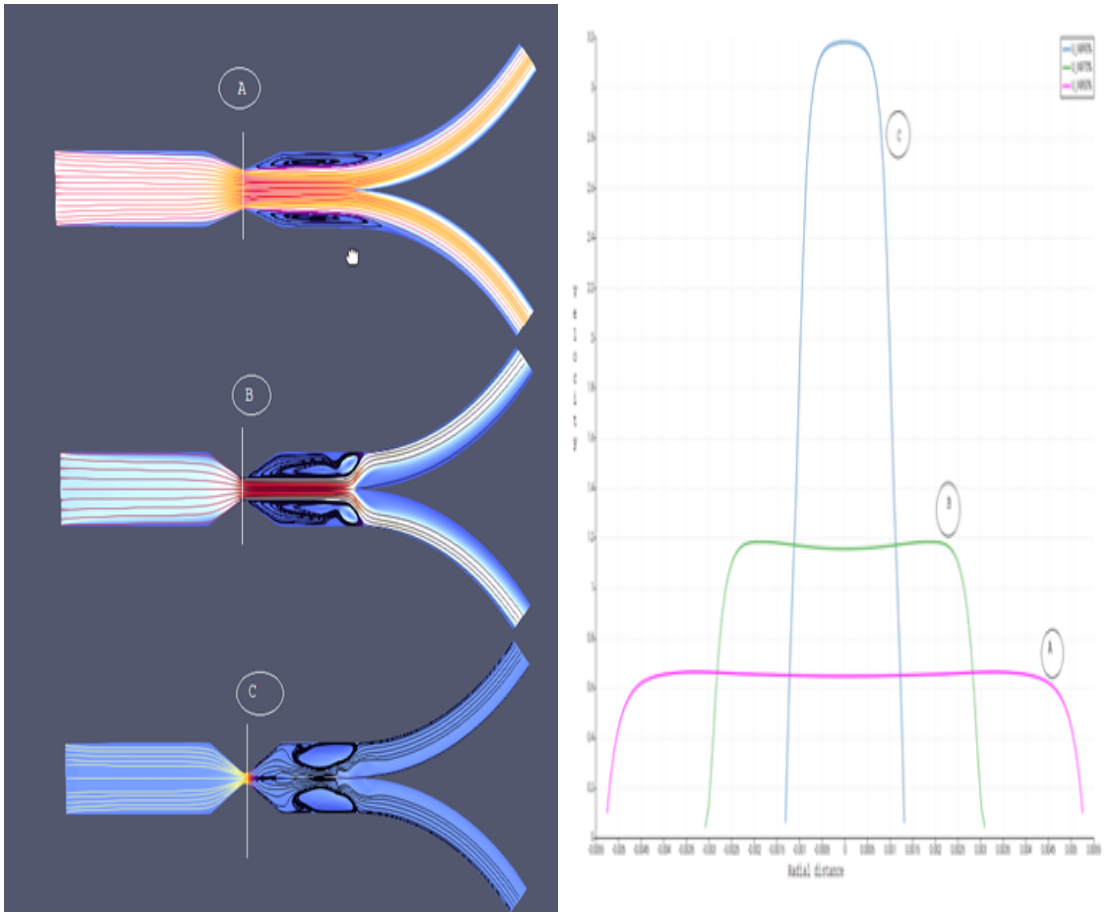

Figure 5.6: Axial velocity contours and velocity profiles in the vicinity of the stenosis, at $x = 4.5$mm: (A) Case 1, 50% blockage; (B) Case 2, 70% blockage; and (C) Case 3, 90% blockage.

Fig. 5.6 shows the axial velocity profiles in the parent artery at a specific location, $x = 4.5$mm for each of the three cases; (A) Case 1, corresponding to a stenosis causing 50% blockage; (B) Case 2, 70% blockage; and (C) Case 3, 90% blockage. We notice that the velocity is directly proportional to the constriction, the higher the blockage, the higher would the velocity 'spurt' through the constriction. This 'spurt' phenomena can be readily demonstrated using the normal garden hose. Water would flow out, i.e. "spurt", at higher speed if one constricts the outlet say with a finger.

This velocity behaviour correspondingly enhances the wall shear-stress as the constriction, due to the stenosis, increases. High wall shear-stresses greatly increase the possibility of rupture of the stenosis/blockage. This can lead to catastrophic consequences in the usual case where the stenosis is caused by tumor growth.

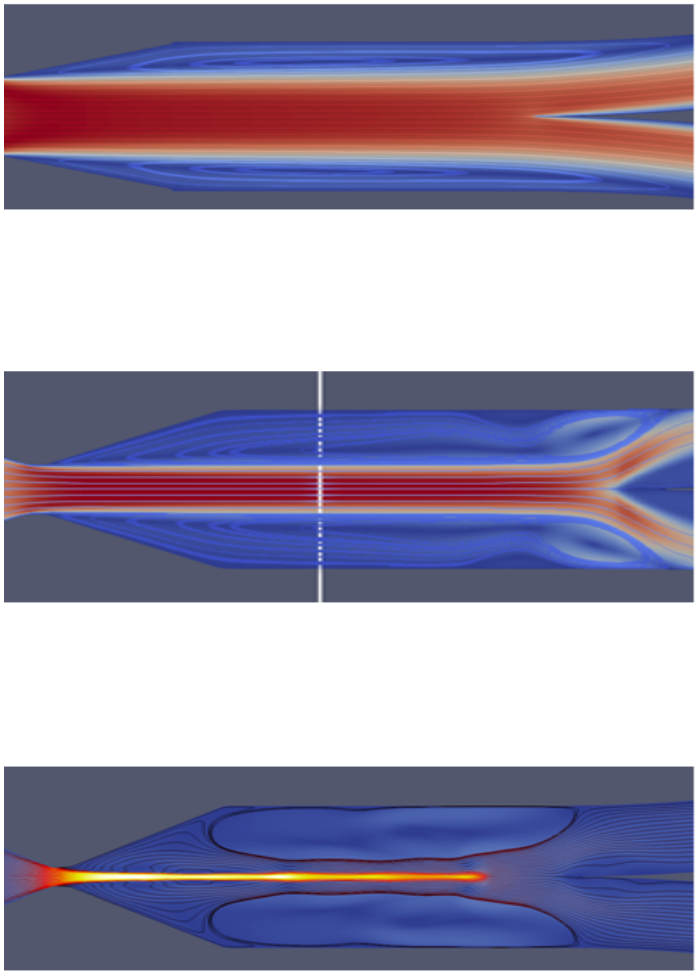

Figure 5.7: Axial velocity contours in the vicinity of the stenosis, at $x = 6.6$mm: (Top) Case 1, 50% blockage; (Middle) Case 2, 70% blockage; and (Bottom) Case 3, 90% blockage.

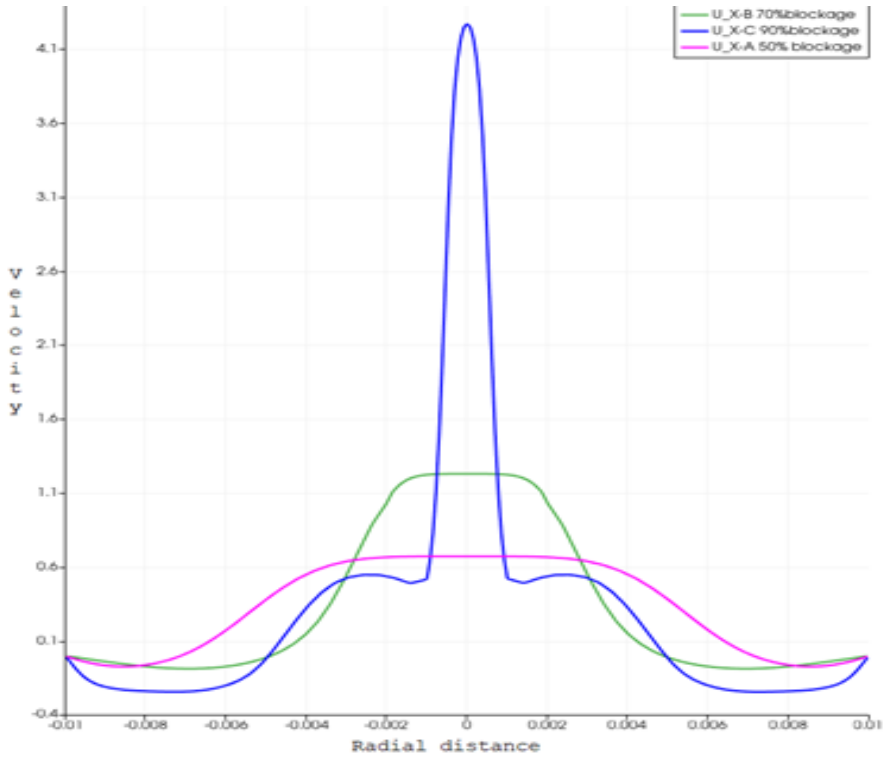

Figure 5.8: Axial velocity profiles in the vicinity of the stenosis, at $x = 6.6$mm: (Magenta) Case 1, 50% blockage; (Green) Case 2, 70% blockage; and (Blue) Case 3, 90% blockage.

Fig. 5.7 shows the axial velocity contours and Fig. 5.8 gives the corresponding velocity profiles in the parent artery at a specific location, $x = 6.6$mm for each of the three cases; Case 1, corresponding to a stenosis causing 50% blockage; Case 2, 70% blockage; and Case 3, 90% blockage. Specifically, Figs. 5.7 and 5.8 illustrates the influence of the severity of stenosis on flow recirculation.

The recirculation zones increase in size as the stenosis becomes more severe. The enhanced vortex formation in direct proportion to the increased severity of the stenosis may lead to a serious complication, such as stenosis/tumor rupture, as a result of the unusual flow reversal characteristics.

Figs. 5.9 through 5.12 illustrate the progression of the velocity profiles as one traverses the bifurcation point starting from the parent branch. The subsequent flow separation is evident, leading to symmetric flow profiles in the daughter branches.

Specifically:

Fig. 5.9 shows the axial velocity profiles just before the bifurcation point. The velocity profile is still continuous but is already being affected by the presence of the bifurcation point.

Fig. 5.10 shows the axial velocity profiles at the bifurcation point. The velocity profile becomes discontinuous due to flow separation resulting from the bifurcation in the channel.

Fig. 5.11 shows the axial velocity profiles just after the bifurcation point. The discontinuous velocity profiles continue to grow further apart as the two daughter branches correspondingly move farther apart as one moves to the right hand side past the bifurcation point.

Fig. 5.12 shows the axial velocity profiles way past the bifurcation point. The distinct velocity profiles continue to independently redevelop inside each of the two daughter branches.

The effects of the stenosis carry into the bifurcation regions. The 'spurt' resulting from more severe blockages continue to ensure correspondingly higher axial velocities.

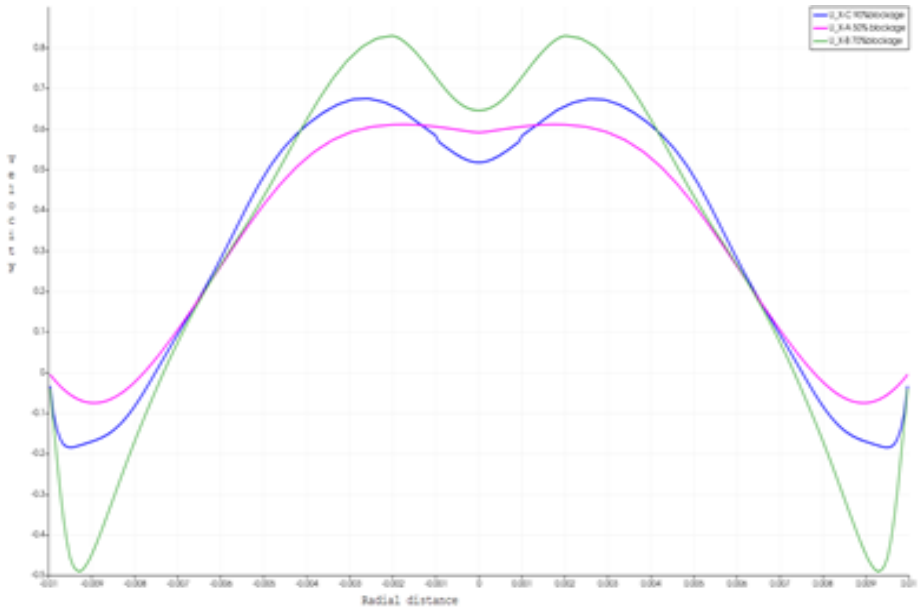

Figure 5.9: Axial velocity profiles just before the bifurcation point: (Magenta) Case 1, 50% blockage; (Green) Case 2, 70% blockage; and (Blue) Case 3, 90% blockage.

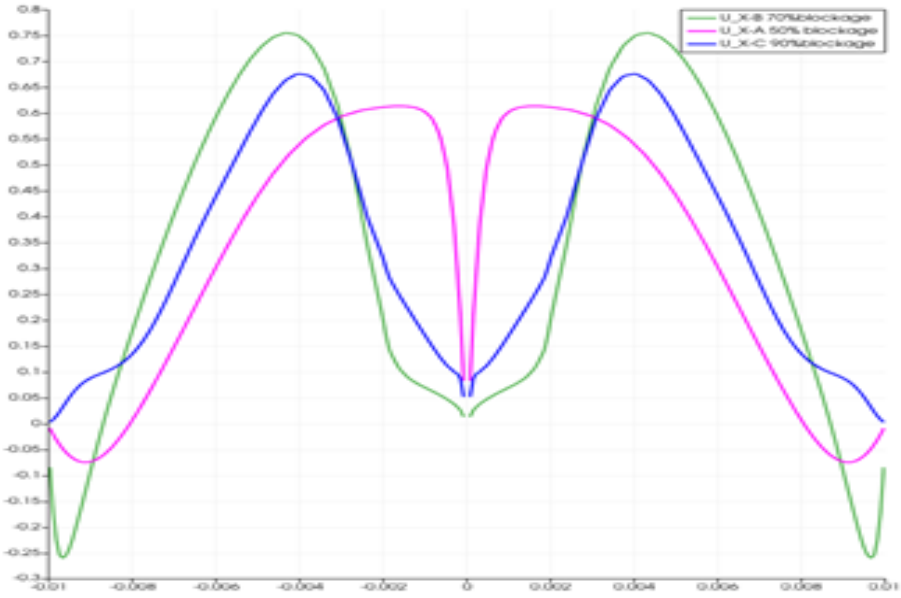

Figure 5.10: Axial velocity profiles at the bifurcation point: (Magenta) Case 1, 50% blockage; (Green) Case 2, 70% blockage; and (Blue) Case 3, 90% blockage.

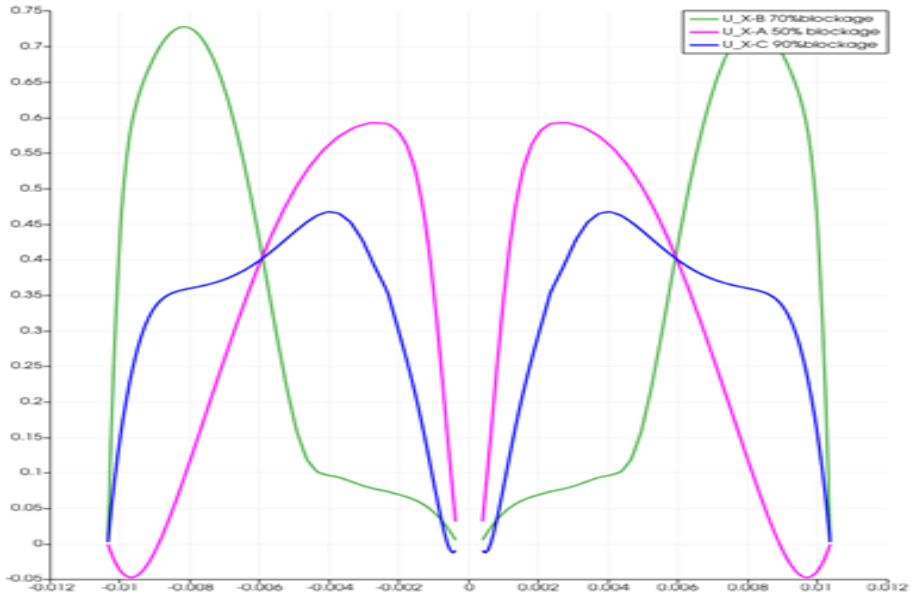

Figure 5.11: Axial velocity profiles just after the bifurcation point: (Magenta) Case 1, 50% blockage; (Green) Case 2, 70% blockage; and (Blue) Case 3, 90% blockage.

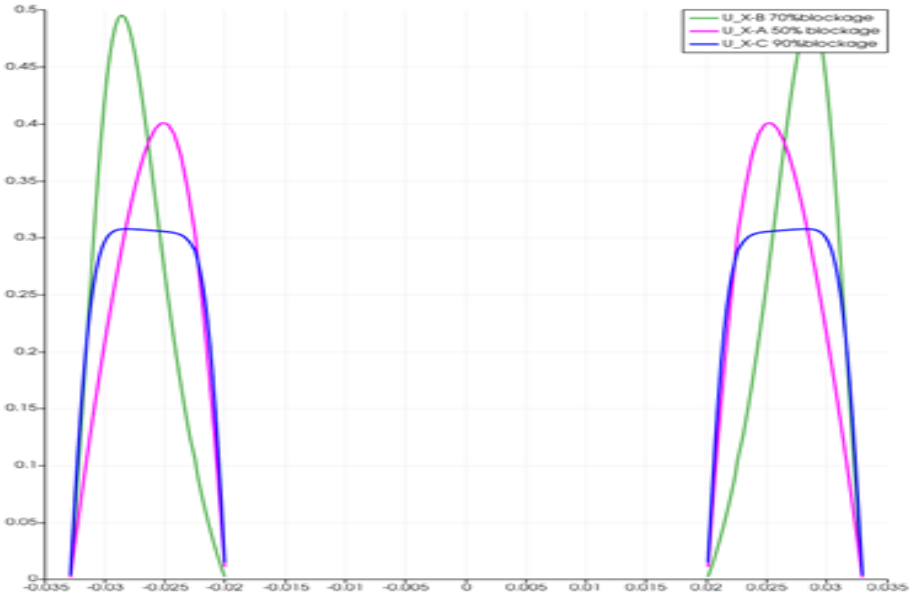

Figure 5.12: Axial velocity profiles way past the bifurcation point, in the daughter branches: (Magenta) Case 1, 50% blockage; (Green) Case 2, 70% blockage; and (Blue) Case 3, 90% blockage.

The normal stress difference results are presented in Figs. 5.13 through 5.15.

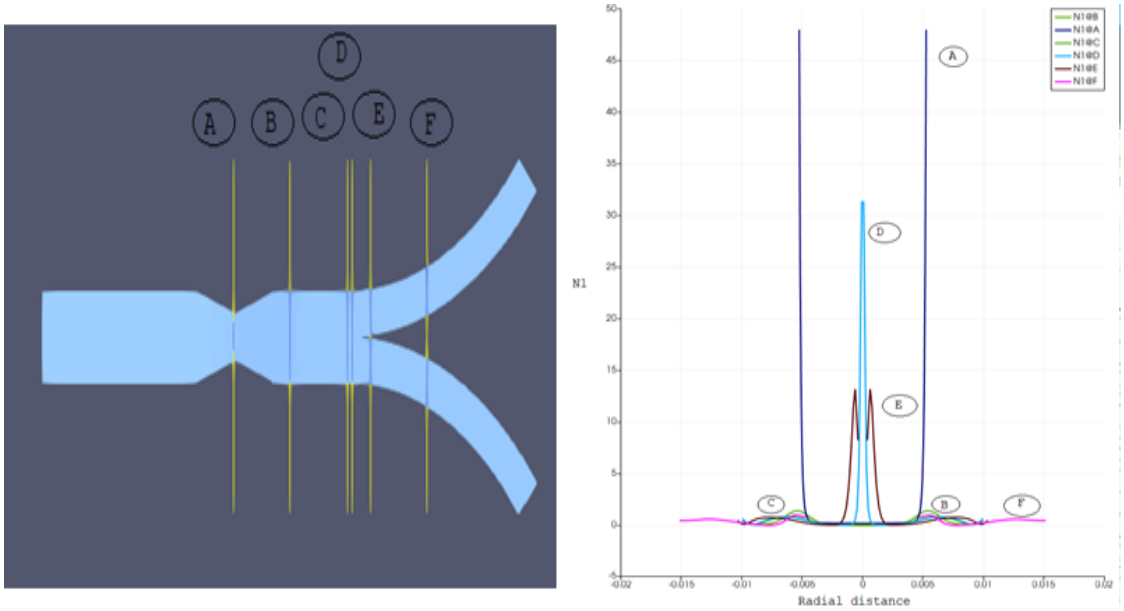

Figure 5.13: Normal stress difference results for stenosis causing 50% blockage.

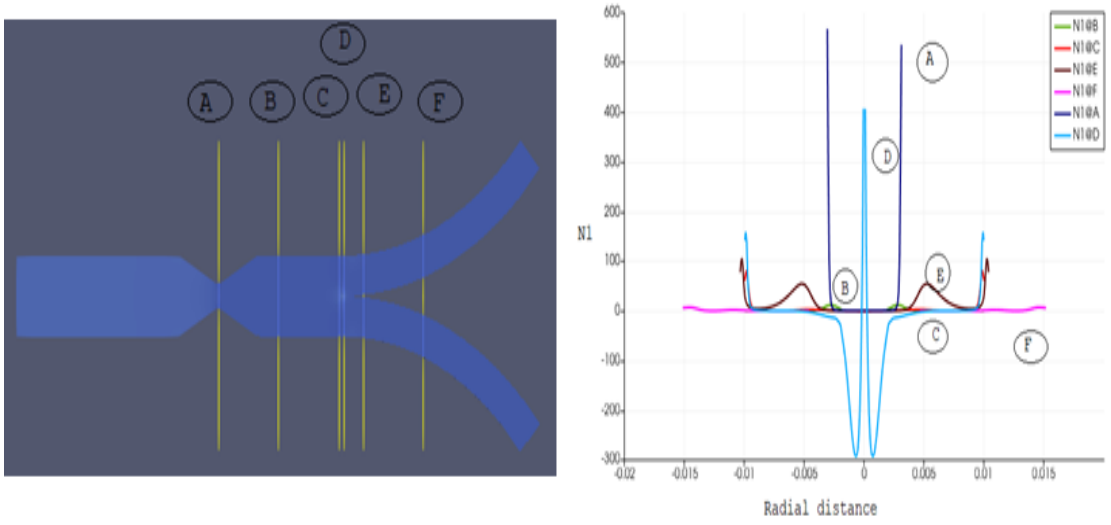

Figure 5.14: Normal stress difference results for stenosis causing 70% blockage.

The blood-pressure results both in the axial and stream-wise direction are presented in Figs. 5.16 through 5.17. During rigorous exercise and similar high blood pressure

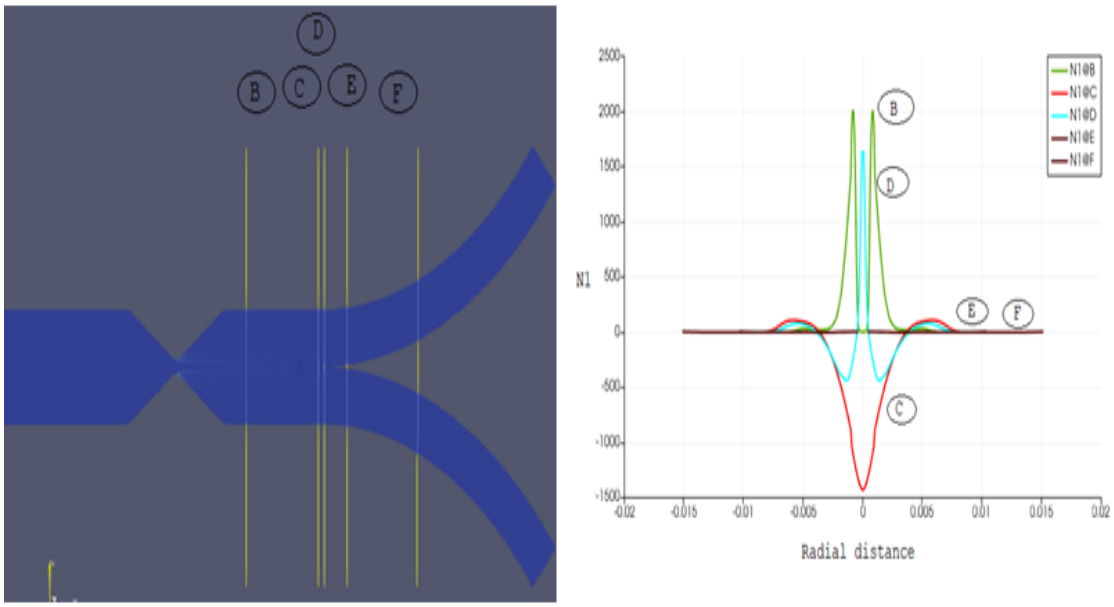

Figure 5.15: Normal stress difference results for stenosis causing 90% blockage.

conditions, elevated levels of the blood velocity magnitudes and resultant wall shear-stresses are observed within the stenosed artery. The maximum pressure values are observed at the higher constriction rates (i.e. the 90% blockage) of stenosis. This explains the 'spurt' phenomena that was observed earlier for the velocity behaviour around the stenosis. The values of the pressure drop as one moves downstream away from the stenosis and towards the bifurcation and daughter branches. Higher values of wall shear-stresses and pressure may cause the development of fatigue in the walls of the stenosed artery. Moreover, higher pulsatile frequencies due to high blood-pressure, under rigorous exercise conditions, may equally increases fatigue.

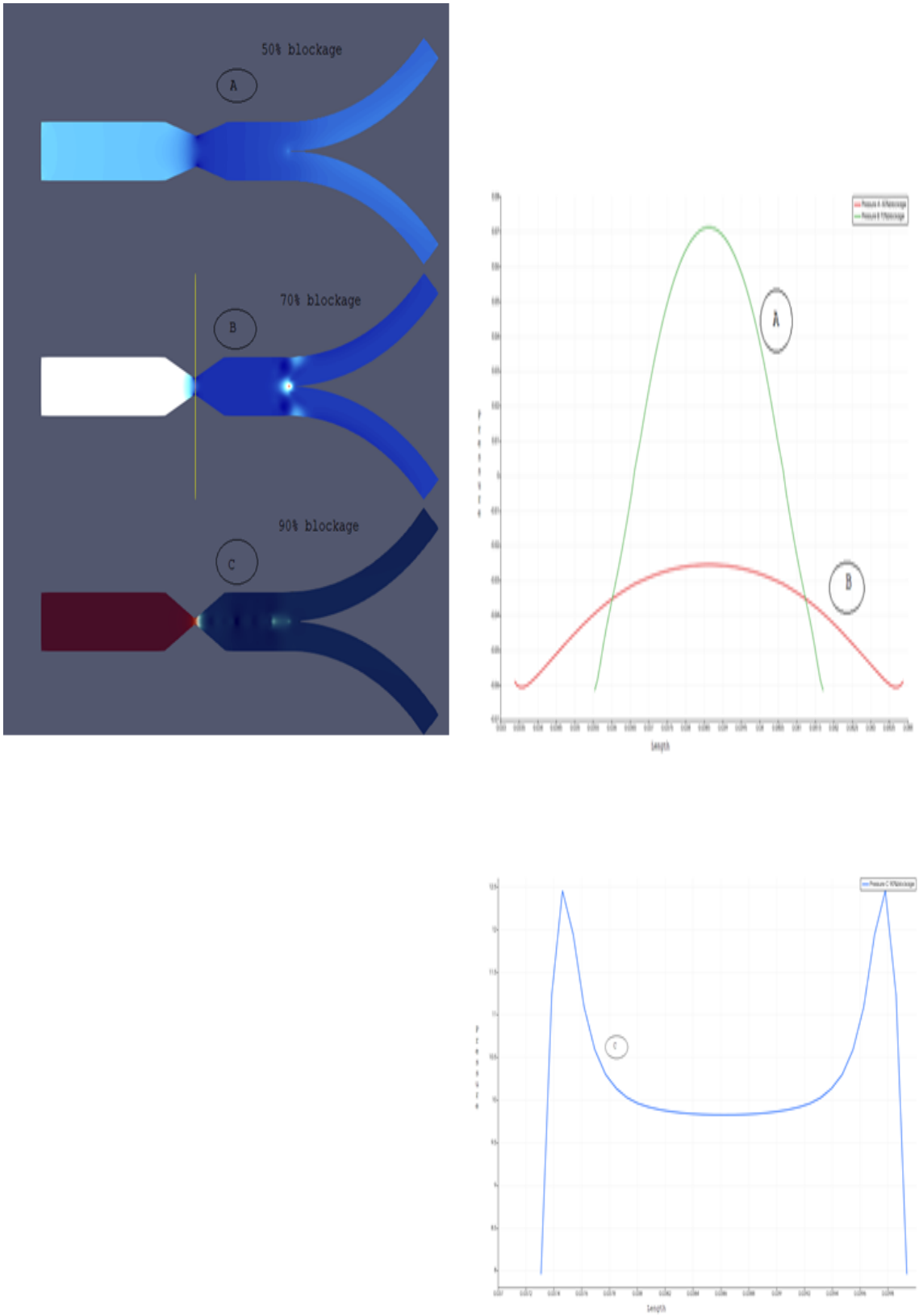

Figure 5.16: Pressure contours in the vicinity of stenosis: (A) 50% blockage; (B) 70% blockage; and (C) 90% blockage.

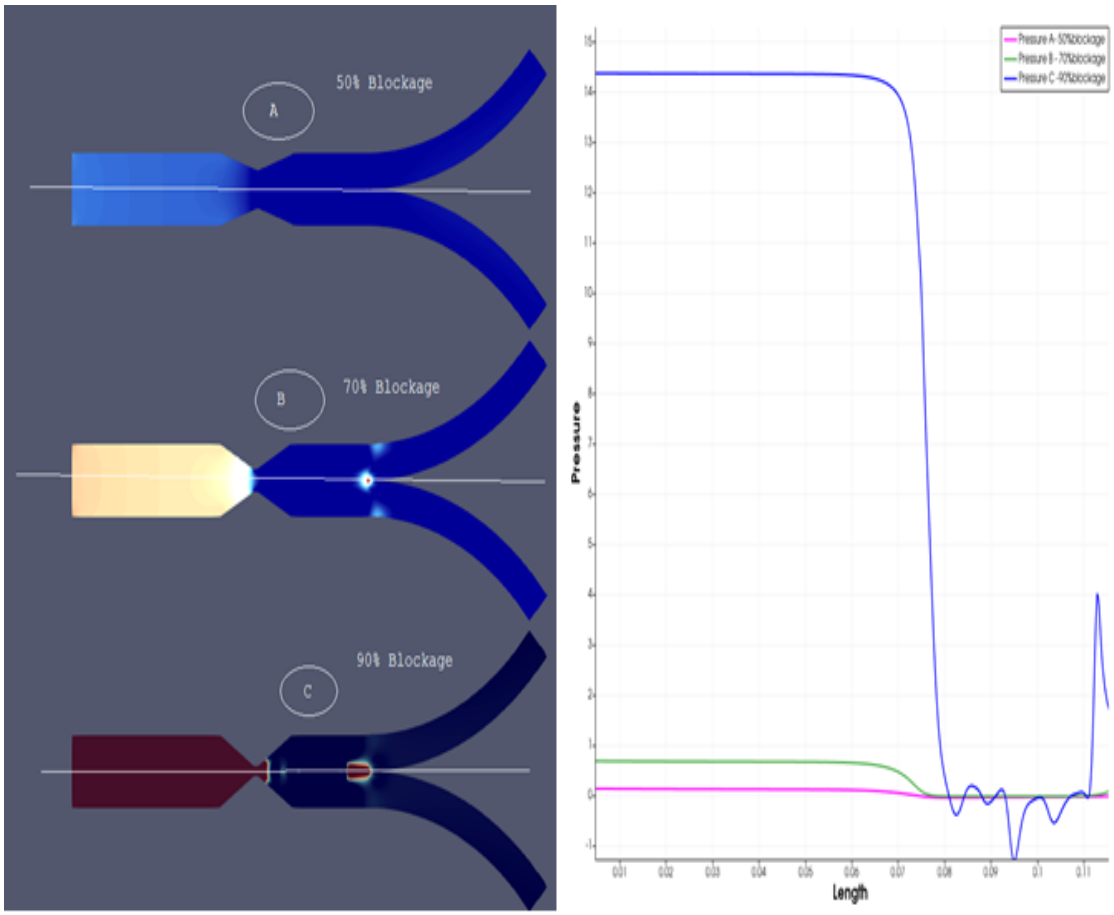

Figure 5.17: Pressure contours along length of stenosed artery: (A) 50% blockage; (B) 70% blockage; and (C) 90% blockage.

In the present chapter, an Oldroyd-B model of blood is adopted to investigate the blood flow characteristics in a stenosed and bifurcating artery. The next chapter extends this work to Generalized Oldroyd-B models for blood in order to additionally account for experimentally observed shear-dependent viscosity.

Chapter 6

Generalized Oldroyd-B modelling of blood flow in stenosed and bifurcating arteries

6.1 Flow geometry

We use the same geometry, see Fig. 5.1, as for the Oldroyd-B model from the previous chapter. The blood flow is again assumed steady, laminar, incompressible, isothermal, and of homogeneous concentration.

6.2 Flow assumptions

Table 6.1 gives a list of the initial values for the blood flow problem using the Generalized Oldroyd-B model.

The following boundary conditions are implemented.

Table 6.1: Initial flow conditions for Generalized Oldroyd-B model

Variable	Initial value
Velocity (U)	$0.33\,\mathrm{m/s}$
Density (ρ)	$1050.87\,\mathrm{kg/m^3}$
Solvent viscosity (η_s)	$0.0067\,\mathrm{kg\,m^{-1}\,s^{-1}}$
Polymer viscosity (η_p)	$0.0017\,\mathrm{kg\,m^{-1}\,s^{-1}}$
Relaxation time (λ)	$0.015\,\mathrm{s}$
Giesekus nonlinear parameter (α)	3.736
Shear-thinning parameters (m and b)	0.254
Reynolds Number (Re)	231

- Wall boundary conditions: the no-slip conditions for the velocity are employed.
- Channel centerline: the symmetry condition for the velocity is enforced.
- Channel inlet: the velocity value is obtained by dividing the prescribed downstream average velocity by four and the stress tensor is considered null.
- Channel outlet: the velocity gradient along the x-direction, as with the pressure, are taken as zero. The zero-gradient boundary condition is used for the polymer stresses.

6.3 Mesh generation

The flow geometry and its corresponding meshing are generated via OpenFOAM's blockMeshdict and blockMesh utilities, see Figs. 6.1 and 6.2.

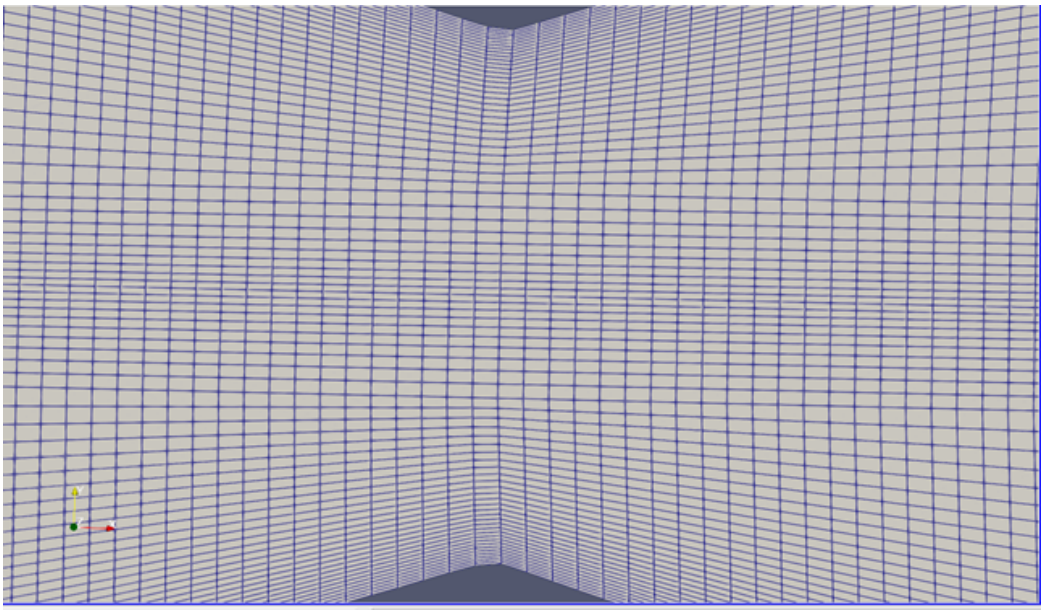

Figure 6.1: Mesh generation via blockMesh around stenosis region.

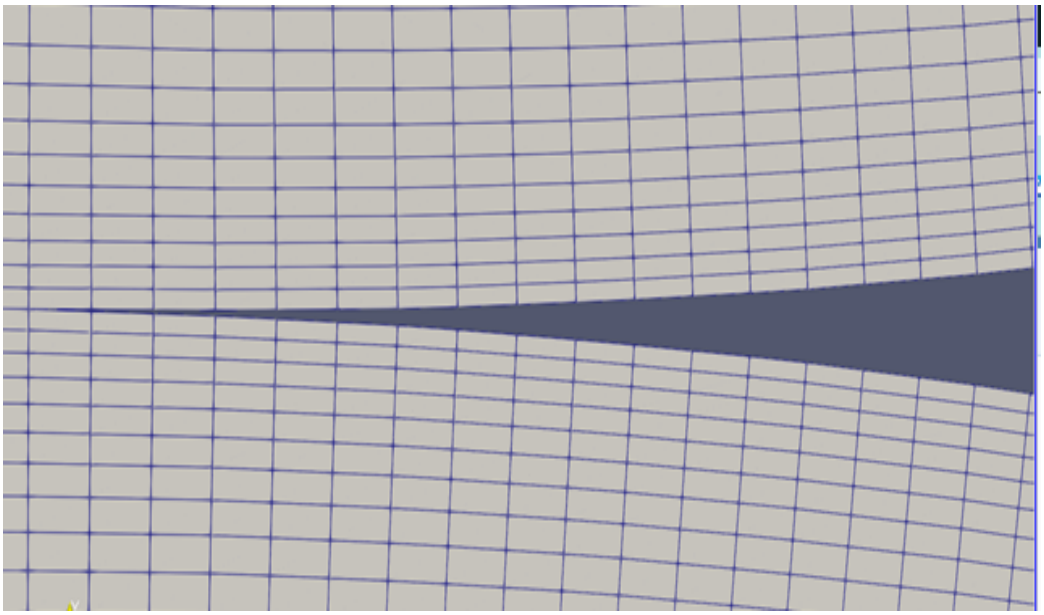

Figure 6.2: Mesh generation via blockMesh around bifurcation zone.

6.4 Generalized Oldroyd-B Results

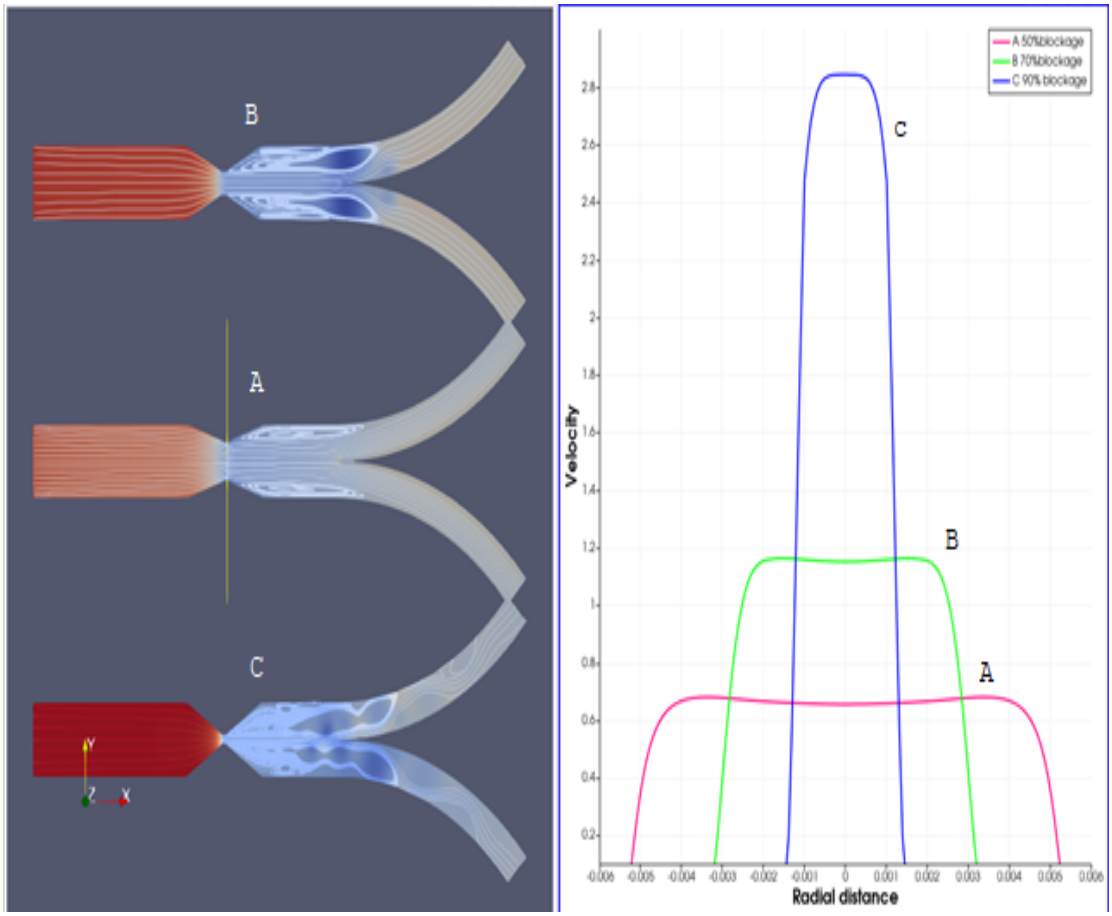

Figure 6.3: Axial velocity contours and velocity profiles in the vicinity of the stenosis, at $x = 4.5$mm: (A) Case 1, 50% blockage; (B) Case 2, 70% blockage; and (C) Case 3, 90% blockage.

The Generalized Oldroyd-B results in Fig. 6.3 (at $x = 4.5$mm) are qualitatively similar to those for the Oldroyd-B model as presented in Fig. 5.6.

The Generalized Oldroyd-B results at $x = 6.6$mm are illustrated in Fig. 6.4. Figs. 6.5 through 6.8 illustrate the progression of the velocity profiles as one traverses the bifurcation point starting from the parent branch. The subsequent flow separation is evident, leading to symmetric flow profiles in the daughter branches.

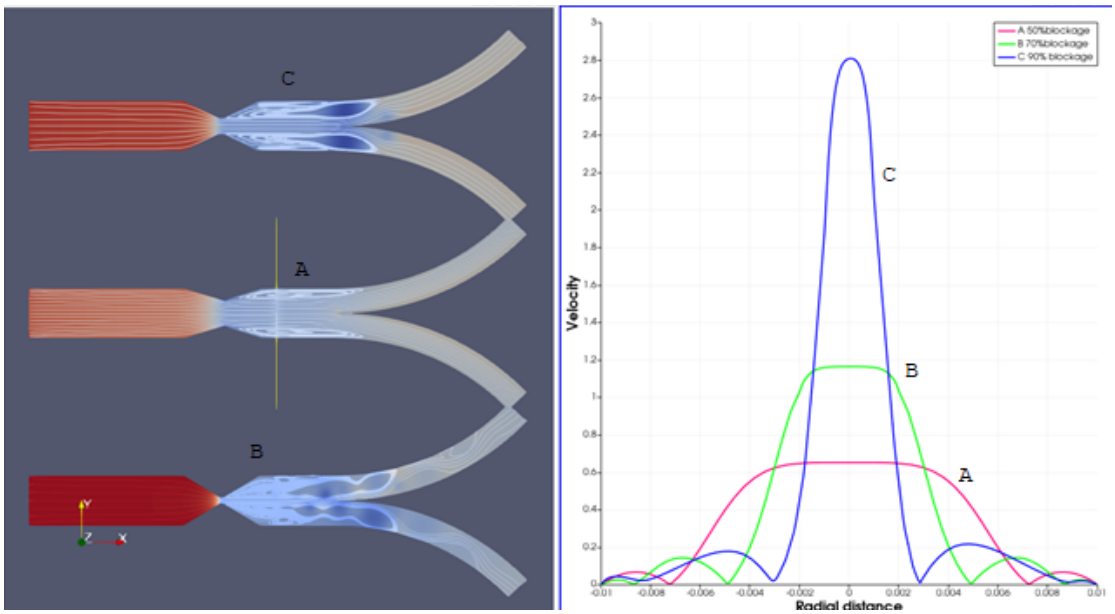

Figure 6.4: Axial velocity contours and velocity profiles in the vicinity of the stenosis, at $x = 6.6$mm: (A) Case 1, 50% blockage; (B) Case 2, 70% blockage; and (C) Case 3, 90% blockage.

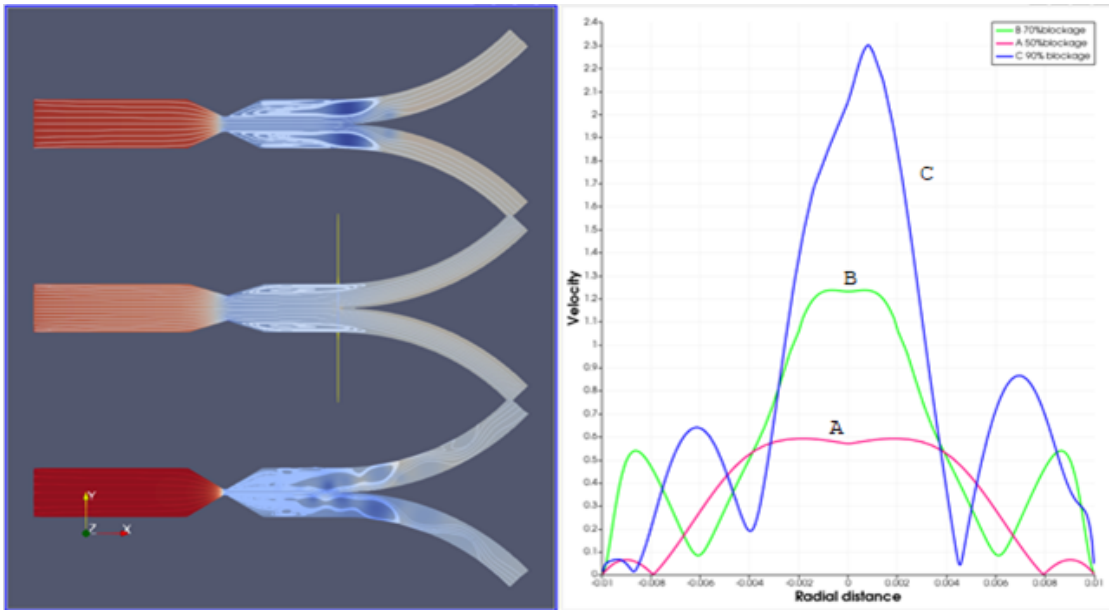

Figure 6.5: Axial velocity contours and velocity profiles just before the bifurcation point: (A) Case 1, 50% blockage; (B) Case 2, 70% blockage; and (C) Case 3, 90% blockage.

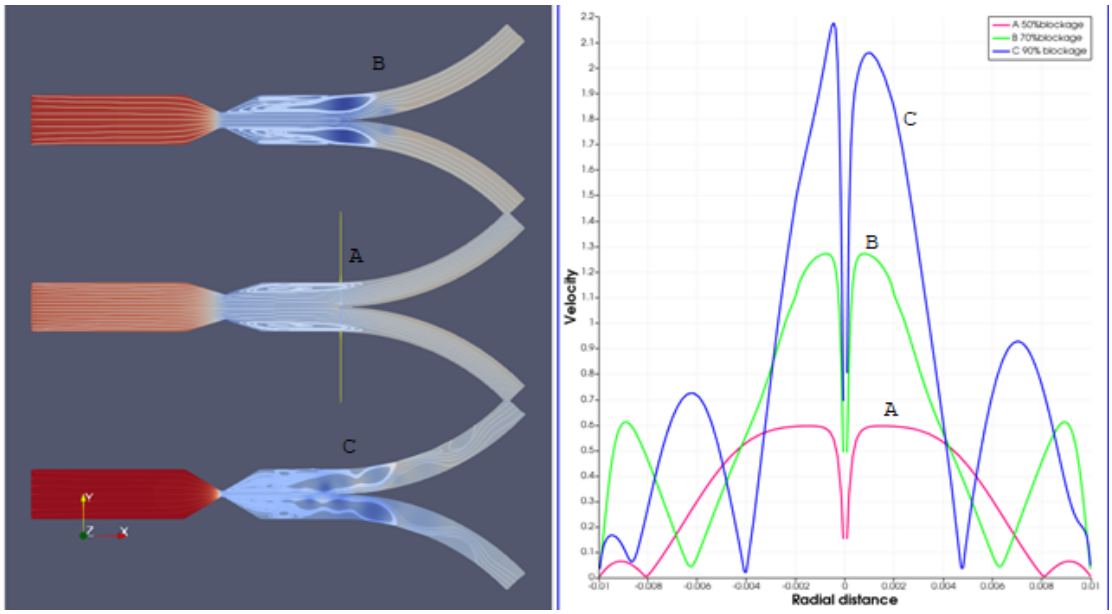

Figure 6.6: Axial velocity contours and velocity profiles at the bifurcation point: (A) Case 1, 50% blockage; (B) Case 2, 70% blockage; and (C) Case 3, 90% blockage.

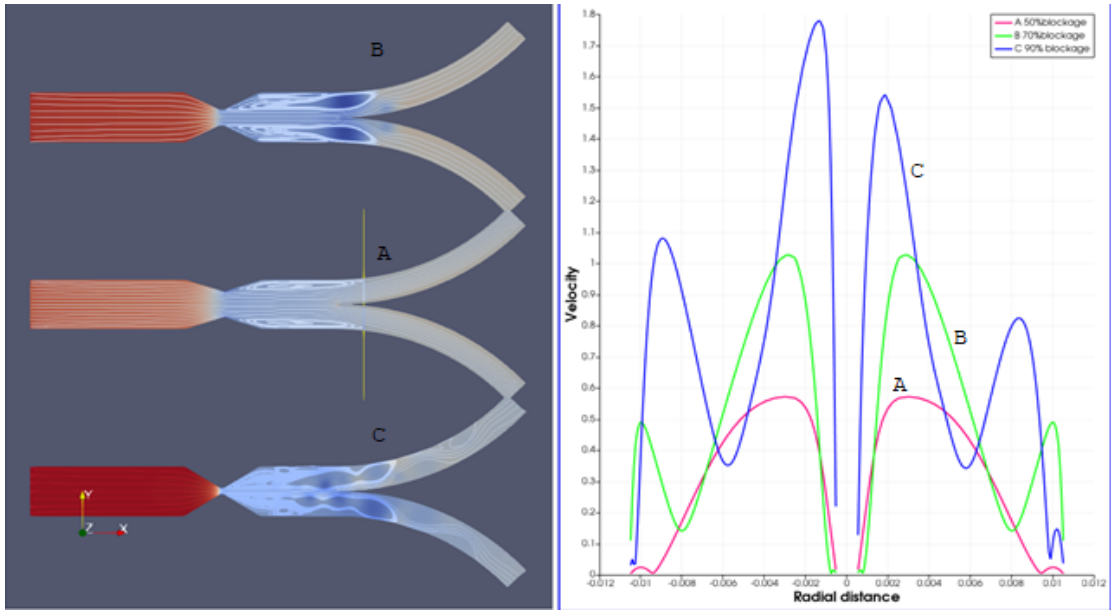

Figure 6.7: Axial velocity contours and velocity profiles just after the bifurcation point: (A) Case 1, 50% blockage; (B) Case 2, 70% blockage; and (C) Case 3, 90% blockage.

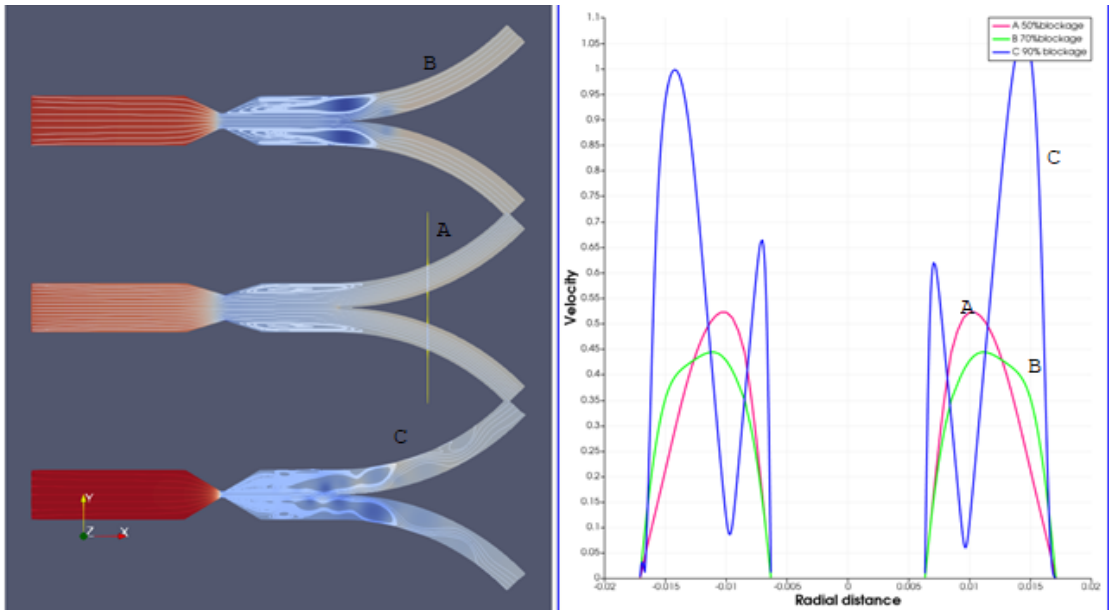

Figure 6.8: Axial velocity contours and velocity profiles deep within the daughter branches, way past the bifurcation point: (A) Case 1, 50% blockage; (B) Case 2, 70% blockage; and (C) Case 3, 90% blockage.

The normal stress difference results are presented in Figs. 6.10 through 6.15.

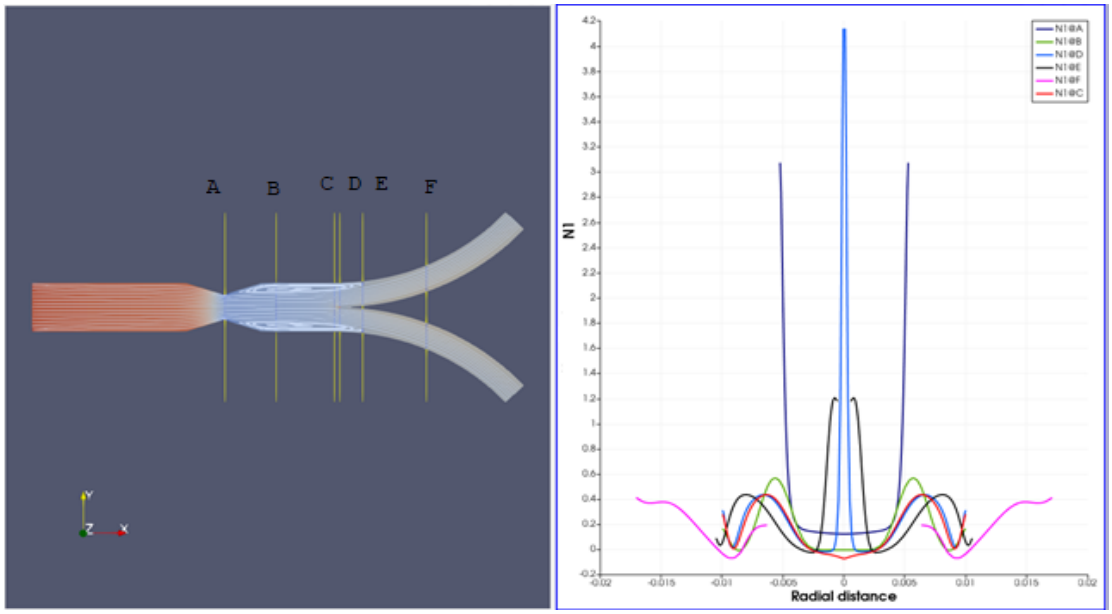

Figure 6.9: Normal stress difference results for stenosis causing 50% blockage.

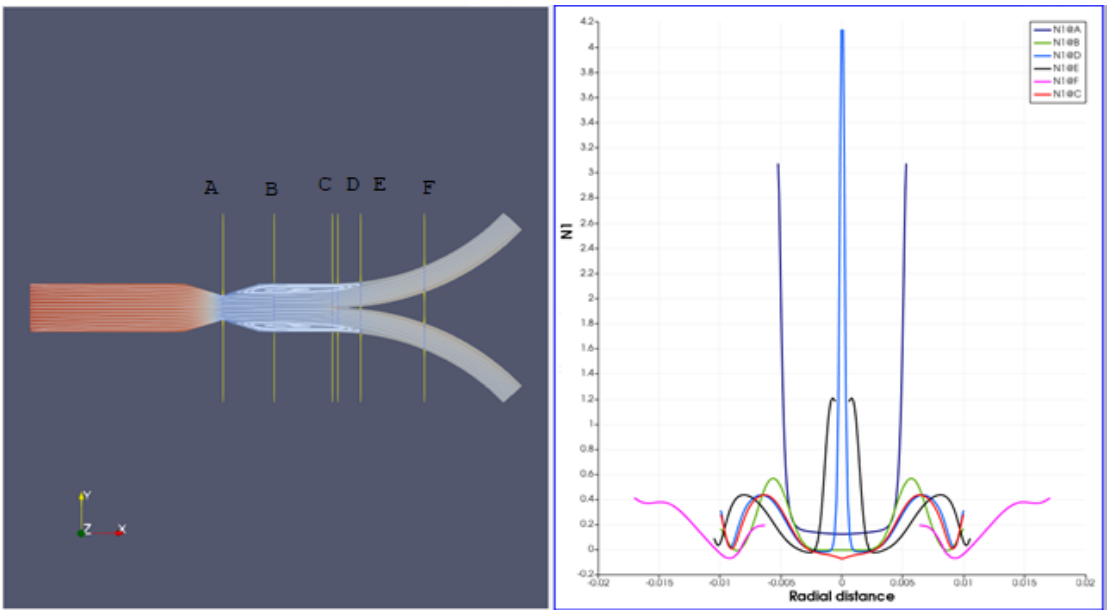

Figure 6.10: Normal stress difference results for stenosis causing 50% blockage.

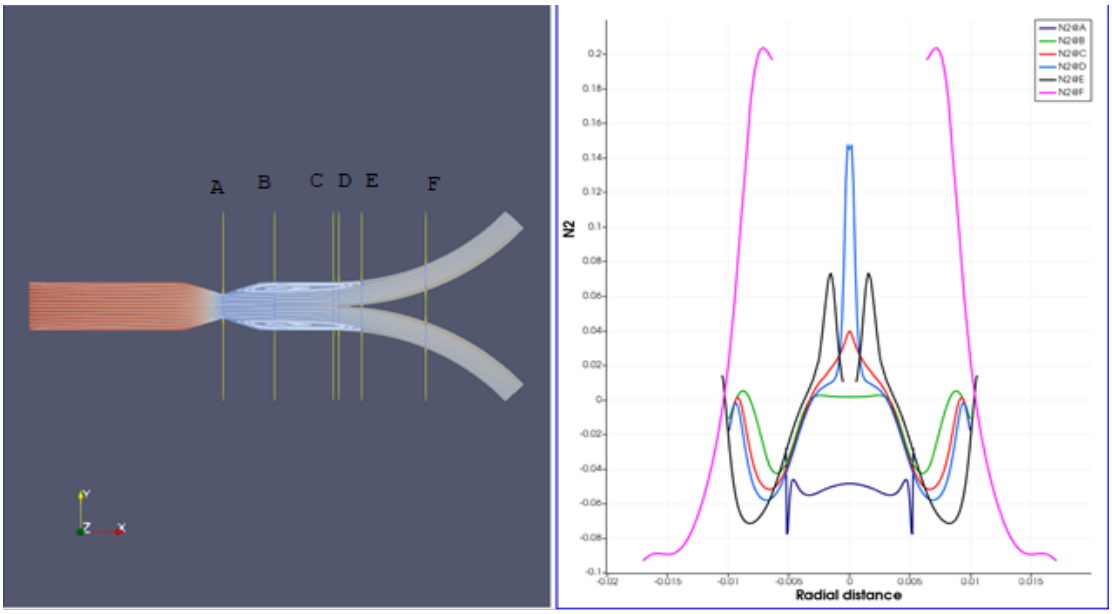

Figure 6.11: Normal stress difference results for stenosis causing 70% blockage.

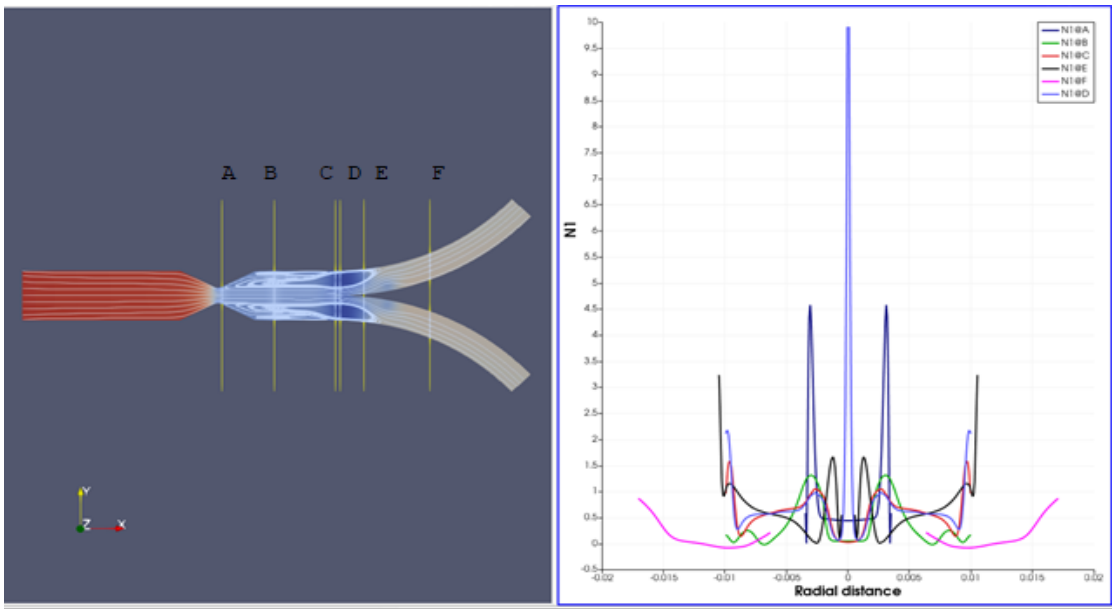

Figure 6.12: Normal stress difference results for stenosis causing 70% blockage.

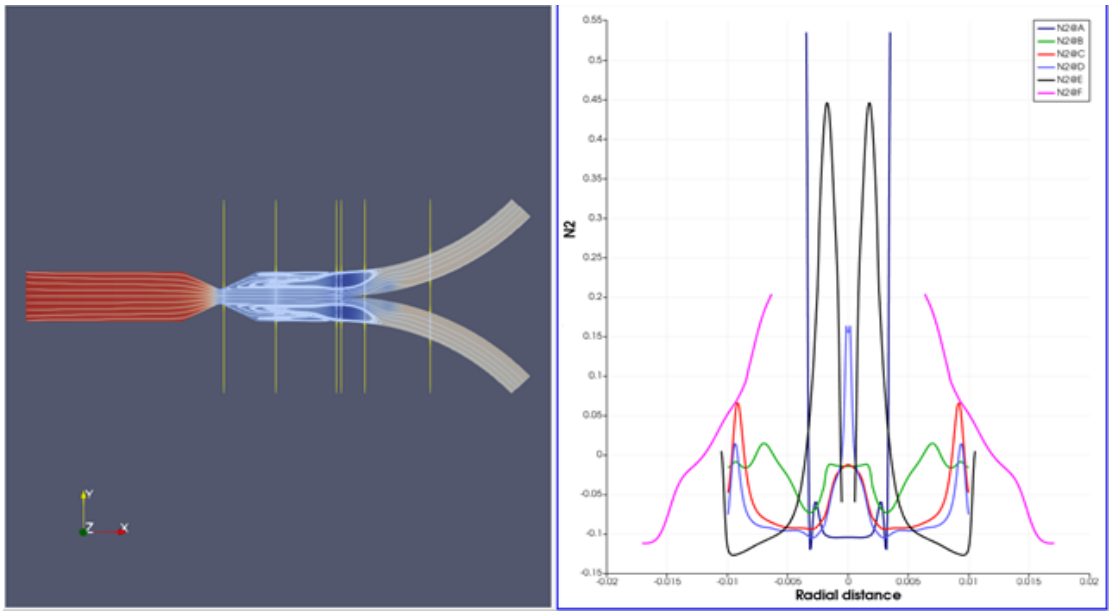

Figure 6.13: Normal stress difference results for stenosis causing 90% blockage.

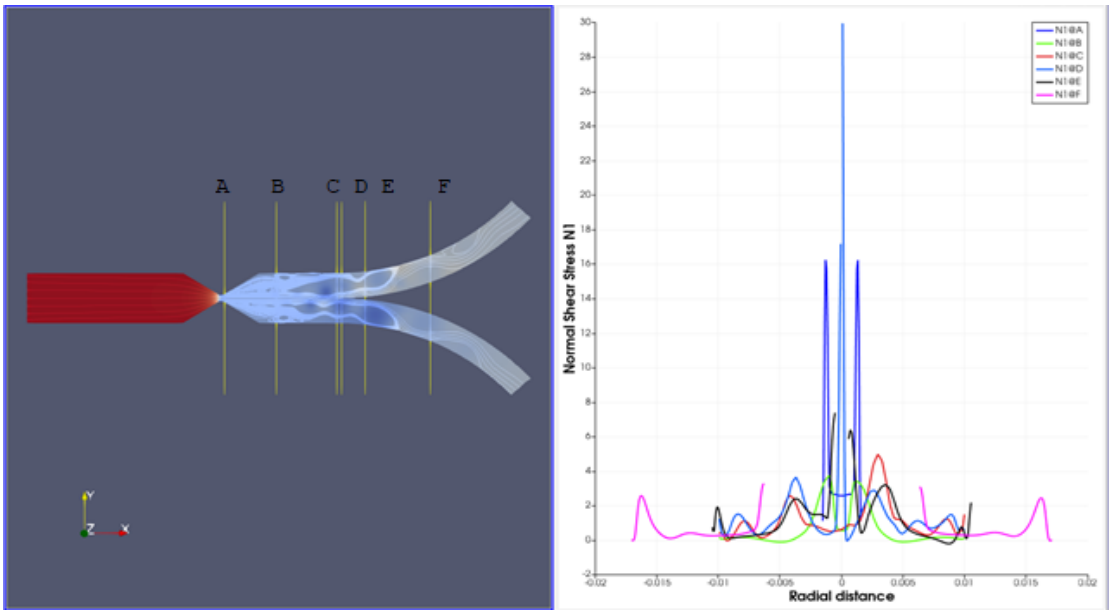

Figure 6.14: Normal stress difference results for stenosis causing 90% blockage.

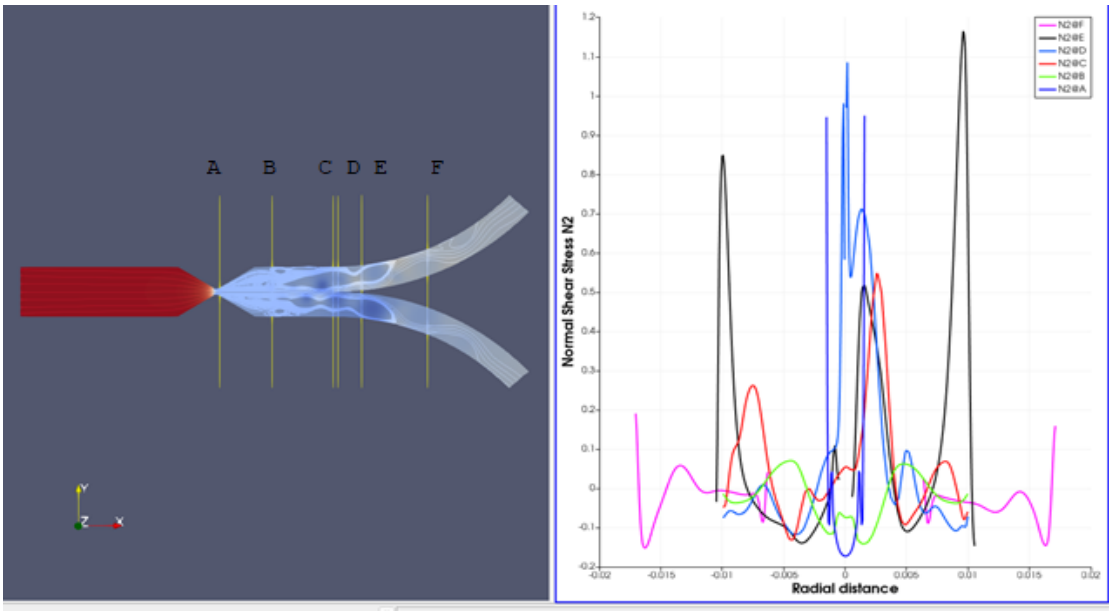

Figure 6.15: Normal stress difference results for stenosis causing 90% blockage.

The blood-pressure profiles are presented in Figs. 6.16 through 6.19.

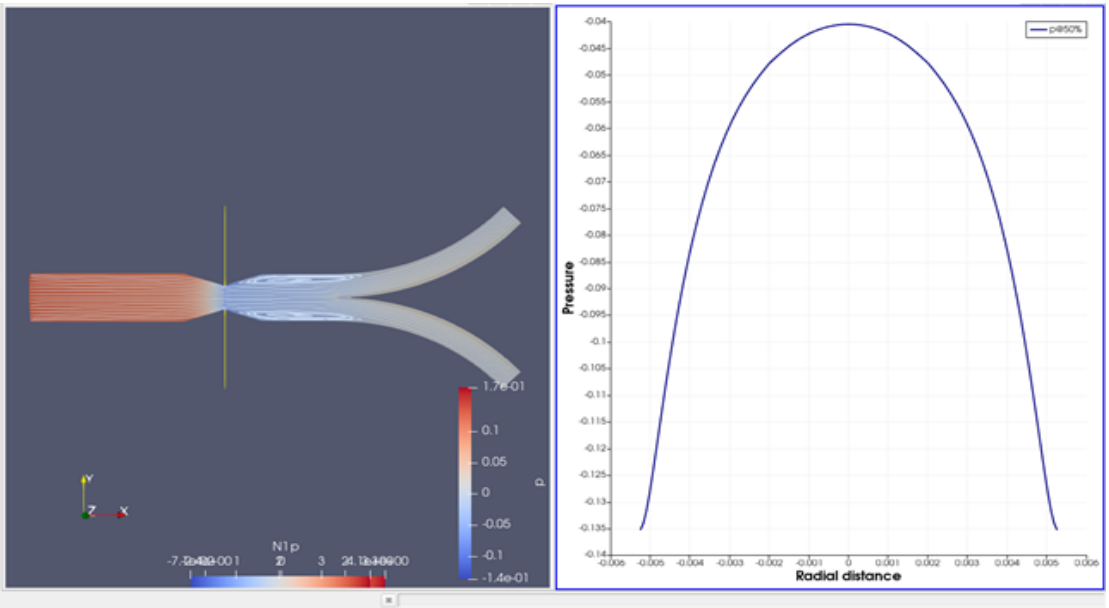

Figure 6.16: Pressure contours in the vicinity of stenosis at 50% blockage.

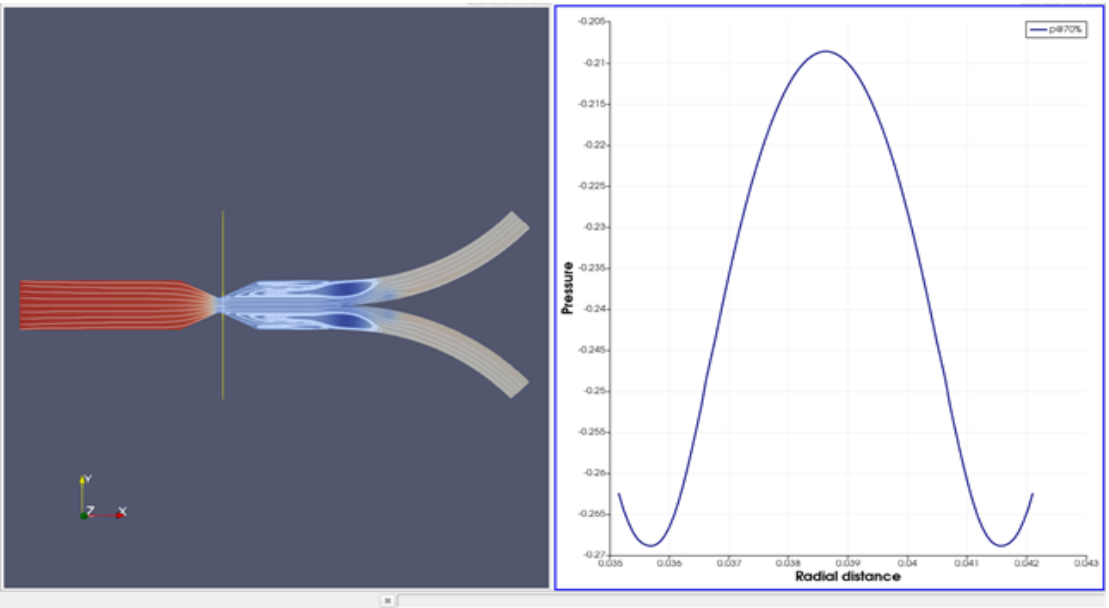

Figure 6.17: Pressure contours in the vicinity of stenosis at 70% blockage.

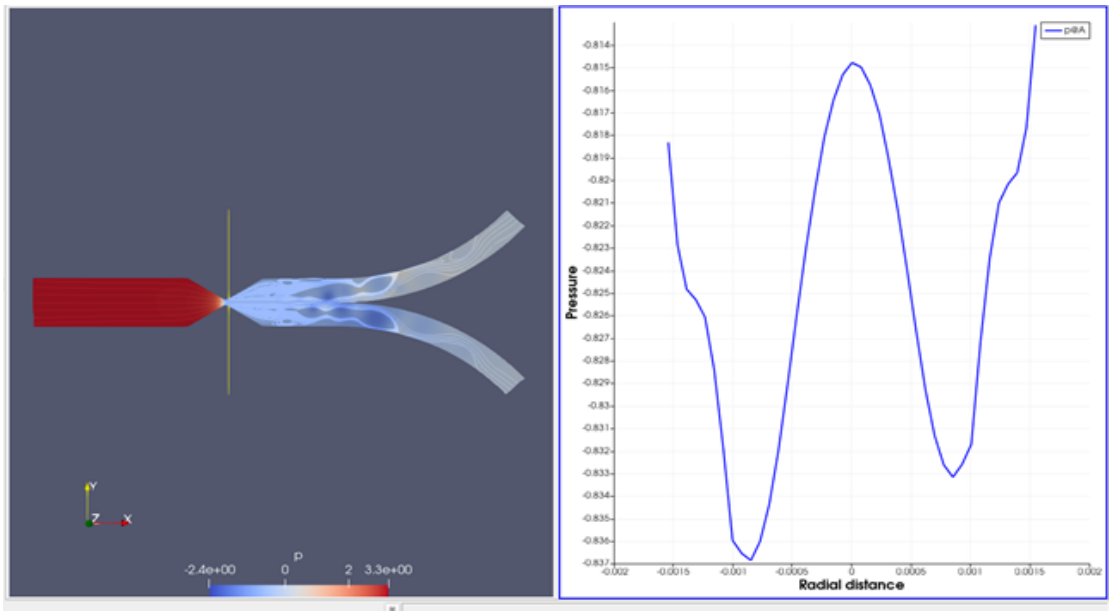

Figure 6.18: Pressure contours in the vicinity of stenosis at 90% blockage.

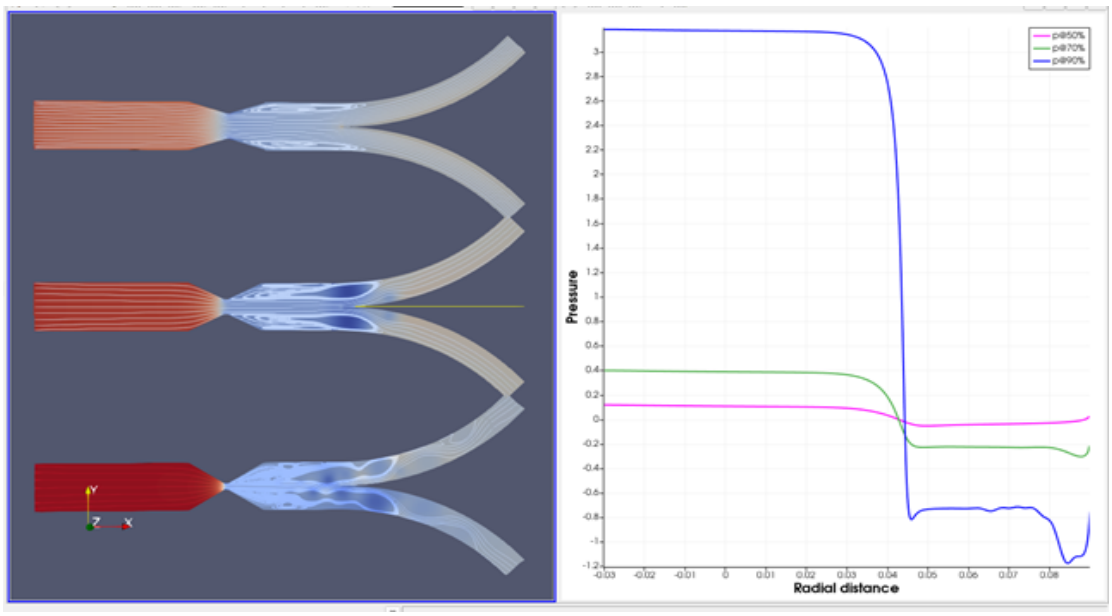

Figure 6.19: Pressure contours along length of stenosed artery: (Top-left) 50% blockage; (Middle-left) 70% blockage; and (Bottom-left) 90% blockage.

Chapter 7

Oldroyd-B versus Generalized Oldroyd-B results

Fig. 7.1 shows the comparative axial velocity profiles for the Oldroyd-B (OB) and Generalized Oldroyd-B (GOB) models in the vicinity of the stenosis using the parameter values already presented in the previous chapter for the Generalized Oldroyd-B model. These results are further presented comparatively via the three stenosis blockage values of 50%, 70%, and 90%.

The results are comparable at lower blockage values but noticeable differences are observed for the higher velocity regime corresponding to large a stenosis blockage. The differences are attributable to the constant (OB) versus shear-dependent (GOB) viscosities as was demonstrated in the 4:1 contraction problem.

Fig. 7.2 shows the comparative blood-pressure profiles for the Oldroyd-B and Generalized Oldroyd-B models in the vicinity of the stenosis at 50% stenosis blockage. Fig. 7.3 shows the comparative blood-pressure profiles for the Oldroyd-B and Generalized Oldroyd-B models along the length of the artery at 50% stenosis blockage.

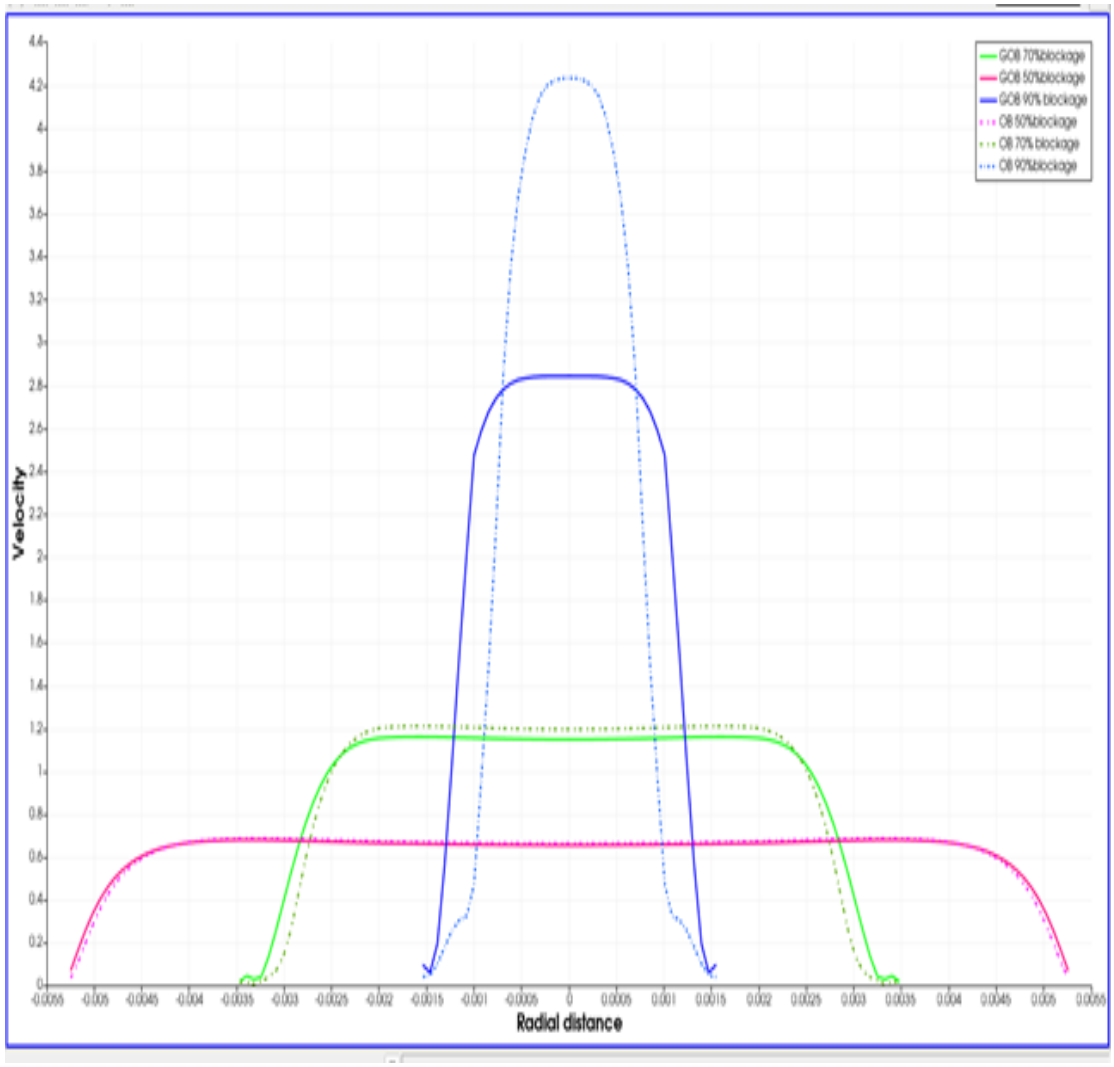

Figure 7.1: Comparison of velocity profiles between Oldroyd-B and Generalized Oldroyd-B models in the vicinity of the stenosis: (blue) 50% blockage; (green) 70% blockage; and (magenta) 90% blockage.

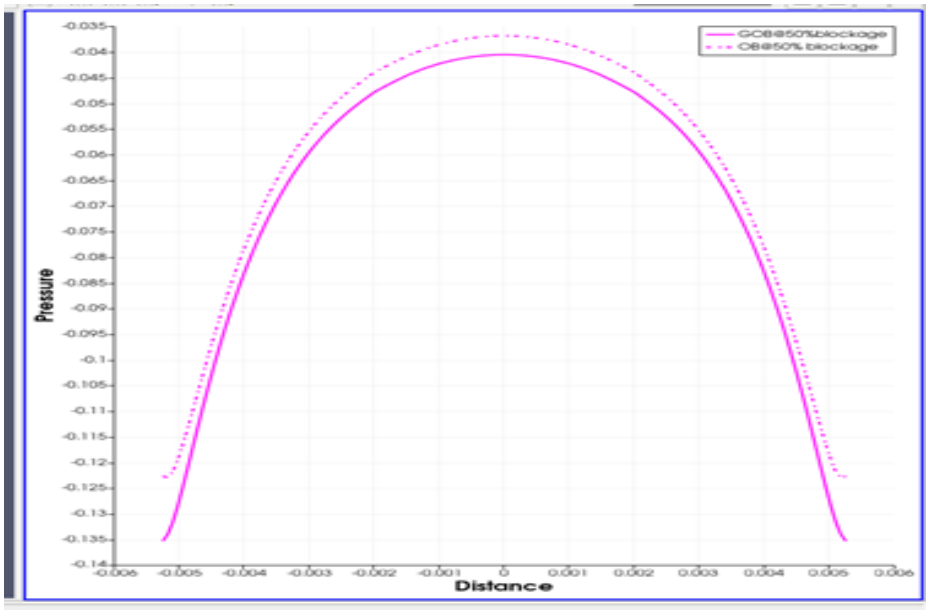

Figure 7.2: Comparison of blood-pressure profiles between Oldroyd-B and Generalized Oldroyd-B models in the vicinity of the stenosis at 50% stenosis blockage.

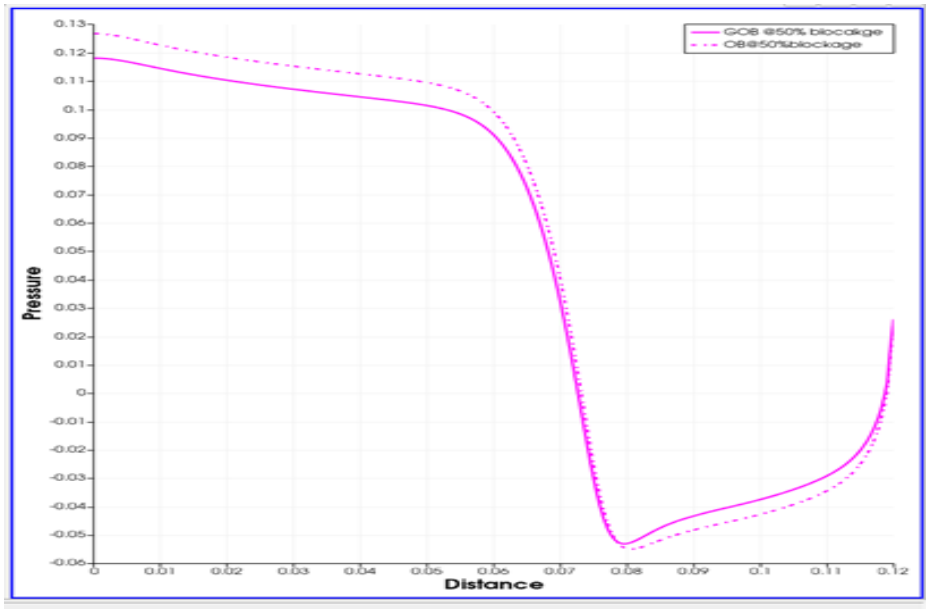

Figure 7.3: Comparison of blood-pressure profiles between Oldroyd-B and Generalized Oldroyd-B models along the length of the artery at 50% stenosis blockage.

Chapter 8

Concluding Remarks

Blood flow simulations are conducted based on the finite volume methods (FVM) implemented on the OpenFOAM software platform. The choice of the OpenFOAM software as platform for the development of the FVM numerical solvers proved to be adequate as it allowed for a clear, straightforward, and numerically stable incorporation of the set of complex differential constitutive models and governing equations. The present work took advantage of the availability of a reasonable set of viscoelastic constitutive model solvers within OpenFOAM, specifically the viscoelasticFluidFoam solver which we modified and developed to suit our focused needs for blood flow computations. The modified viscoelasticFluidFoam solver was implemented stably, to mitigate against the high Weissenberg number problem, and efficiently to reduce computational costs. The modified computational algorithms were successfully validated against well-known benchmark flow problems in the literature. Noting that the Giesekus viscoelastic constitutive model is a generalization of both the Oldroyd-B and Generalized Oldroyd-B models, the validation exercise were naturally conducted via the Giesekus model. This allowed for the development of a general purpose code for fluids described by any of these three viscoelastic

constitutive models. Indeed, benchmark results were also then presented for both the Oldroyd-B and Generalized Oldroyd-B models.

The constitutive models presented in this paper show optimal convergence trends during the nonlinear iterations. Such convergence trends are maintained as the inflow velocity is gradually increased. This super-linear convergence is attributed to the smoother transition in the internal constitutive variables at low shear-rates.

From both the Oldroyd-B and Generalized Oldroyd-B results, it was observed that the velocity is directly proportional to the constriction caused by the stenosis. The higher the blockage from the constriction, the higher would the velocity spurt through the constriction. This velocity behaviour correspondingly enhances the wall shear-stress as the constriction increases, caused by the presence of the stenosis. High wall shear-stresses greatly increase the possibility of rupture of the stenosis/blockage. This can lead to catastrophic consequences in the usual case where the stenosis is caused by tumor growth.

As demonstrated near the contraction of a 4:1 contraction flow geometry, dramatic fluid flow effects, which are attributable to the polymeric-stresses, specifically to the first normal stress difference, are observed in the vicinity of the constrictions resulting from the presence of the stenosis. Such effects, include, flow recirculation and reversal, vortex formation, and spurt phenomena.

The investigations conducted in this thesis have laid the foundation for important follow-up and future work. A deeper scientific understanding of diseases such as diabetes, which are caused by high sugar concentrations in the blood system, can be directly achieved from a mathematical modelling perspective by adding concentration equations to the constitutive models presented in this thesis. Similarly, a scientific understanding of fever based diseases such as rheumatic heart disease would require the coupling of an energy equation to the constitutive models presented in this

thesis. Our ultimate aim, therefore, is to develop a truly general-purpose code for blood flow modelling that can be used to simulate arterial blood flow under various conditions and indeed under any combination of the various prevailing conditions, say for example the combined presence of tumors, fever, and high concentrations of blood sugars.

Bibliography

[1] R.B. Bird, R.C. Armstrong, and O. Hassager, Dynamics of polymeric liquids: Fluid Mechanics, Vol. 1, Wiley, New York, 1977.

[2] R.B. Bird, R.C. Armstrong, and O. Hassager, Dynamics of polymeric liquids: Fluid Mechanics, Vol. 1, 2nd Ed., Wiley, New York, 1987.

[3] N. Aldi, C. Buratto, N. Casari, D. Dainese, V. Mazzanti, F. Mollica, E. Munari, M. Occari, M. Pinelli, S. Randi, P.R. Spina, A. Suman, Experimental and Numerical Analysis of a Non-Newtonian Fluids Processing Pump, Energy Procedia, 126, 2017, 762-769.

[4] G.B. Thurston, Viscoelasticity of Human Blood, Biophysical Journal, Volume 12, Issue 9, 1972, Pages 1205-1217.

[5] H.A.C. Sánchez, M.R. Jovanović, S. Kumar, A. Morozov, V. Shankar, G. Subramanian, H.J. Wilson, (2022) Understanding viscoelastic flow instabilities: Oldroyd-B and beyond, Journal of Non-Newtonian Fluid Mechanics 302, 104742.

[6] R. Sureshkumar, A.N. Beris, R.A. Handler, Direct numerical simulation of the turbulent channel flow of a polymer solution, Physics of Fluids, 9(3), 1997, 743-755.

[7] M. Kaibara, U. Yasuyuki, S. Mineyoshi, Effects of mechanical trauma of blood cells on dynamic viscoelasticity of blood during clotting, Thrombosis Research, 43(4), 1986, 395.

[8] M.K. Sharp, G.B. Thurston, J.E. Moore, The effect of blood viscoelasticity on pulsatile flow in stationary and axially moving tubes, Biorheology, 33(3), 1996, 185.

[9] E. Li, G.R. Liu, G.X. Xu, T. Vincent, Z.C. He, Numerical modeling and simulation of pulsatile blood flow in rigid vessel using gradient smoothing method, Engineering Analysis with Boundary Elements, 36(3), 2012, 322.

[10] P. Assemat, J.A. Armitage, K.K. Siu, K.G. Contreras, A.M. Dart, J.P. Chin-Dusting, K. Hourigan, Three-dimensional numerical simulation of blood flow in mouse aortic arch around atherosclerotic plaques, Applied Mathematical Modelling, 38(17), 2014, 4175.

[11] K. Yamamoto, R. Sakurai, M. Motosuke, Fully-automatic blood-typing chip exploiting bubbles for quick dilution and detection, Biomicrofluidics, 14(2), 2020, 024111.

[12] E.J. Scully, E. Shabani, G.W. Rangel, C. Grüring, U. Kanjee, M.A. Clark, M. Chaand, R. Kurita, Y. Nakamura, M.U. Ferreira, M.T. Duraisingh, Generation of an immortalized erythroid progenitor cell line from peripheral blood: A model system for the functional analysis of Plasmodium spp. invasion, Am J Hematol, 94(9), 2019, 963-974.

[13] Y.J. Chang, C.Y. Ho, X.M. Zhou, H.R. Yen, Determination of degree of RBC agglutination for blood typing using a small quantity of blood sample in a microfluidic system. Biosens Bioelectron, 102, 2018, 234-241.

[14] https://www.stanfordchildrens.org/en/topic/default?id=what-is-plasma-160-37

[15] A. Bonaventura, L. Liberale, F. Carbone, A. Vecchié, C. Diaz-Cañestro, G.G. Camici, F. Montecucco, F. Dallegri, The Pathophysiological Role of Neutrophil Extracellular Traps in Inflammatory Diseases, Thromb Haemost, 118(1), 2018, 6-27.

[16] R. Kanamaru, H. Ohzawa, H. Miyato, S. Matsumoto, H. Haruta, K. Kurashina, S. Saito, Y. Hosoya, H. Yamaguchi, H. Yamashita, Y. Seto, A.K. Lefor, N. Sata, J. Kitayama, Low density neutrophils (LDN) in postoperative abdominal cavity assist the peritoneal recurrence through the production of neutrophil extracellular traps (NETs), Sci Rep, 8(1), 2018, 632.

[17] T. Chinyoka, Comparative Response of Newtonian and Non-Newtonian Fluids Subjected to Exothermic Reactions in Shear Flow, International Journal of Applied and Computational Mathematics, 7(3), 2021, 1-19.

[18] T. Chinyoka, Viscoelastic effects in double pipe single pass counterflow heat exchangers, International journal for numerical methods in fluids, 59(6), 2009, 677-690.

[19] T. Chinyoka, Modeling of cross-flow heat exchangers with viscoelastic fluids, Nonlinear Analysis: Real World Applications, 10(6), 2009, 3353-3359.

[20] I. Khan, T. Chinyoka, A. Gill, Dynamics of Non-Isothermal Pressure-Driven Flow of Generalized Viscoelastic-Fluid-Based Nanofluids in a Channel, Mathematical Problems in Engineering, vol. 2022, Article ID 9080009, 17 pages, 2022. https://doi.org/10.1155/2022/9080009

[21] I. Khan, T. Chinyoka, A. Gill, Computational Analysis of Shear Banding in Simple Shear Flow of Viscoelastic Fluid-Based Nanofluids Subject to Exothermic Reactions, Energies, 2022, To Appear.

[22] I.E. Ireka, T. Chinyoka, Analysis of shear banding phenomena in non-isothermal flow of fluids governed by the diffusive Johnson-Segalman model, Applied Mathematical Modelling, 40(5-6), 2016, 3843-3859.

[23] H. Giesekus, A simple constitutive equation for polymer fluids based on the concept of deformation-dependent tensorial mobility, Journal of Non-Newtonian Fluid Mechanics, Volume 11, Issues 1–2, 1982, 69-109.

[24] C.F. Curtiss, R.B. Bird, A kinetic theory for polymer melts. I. The equation for the single-link orientational distribution theory, J. Chem. Phys., 74, 1981, 2016-2025.

[25] C.F. Curtiss, R.B. Bird, A kinetic theory for polymer melts. II. The stress tensor and the rheological equation of state, J. Chem. Phys., 74, 1981, 2026-2033.

[26] D. Vlassopoulos, S.G. Hatzikiriakos, A generalized Giesekus constitutive model with retardation time and its association to the spurt effect, Journal of Non-Newtonian Fluid Mechanics, Volume 57, Issues 2–3, 1995, 119-136.

[27] R.G Larson, Constitutive Equations for Polymer Melts and Solutions, Butterworths, Boston (1988).

[28] M.A. Ikbal, S. Chakravarty, K.K.L. Wong, J. Mazumdarb, P.K. Mandala, Unsteady response of non-Newtonian blood flow through a stenosed artery in magnetic field, Journal of Computational and Applied Mathematics, 230, 2009, 243–259.

[29] Y.I. Cho, K.R. Kensey, Effects of Non-Newtonian Viscosity of Blood on Flows in Diseased Arterial Vessel, Part 1: Steady Flows, 28, 1991, 41-262.

[30] M.M. Cross, Rheology of non-Newtonian fluids: A new flow equation for pseudoplastic systems, J. Colloid Sci., 20(5), 1965, 417-437.

[31] S.C. Hauswirth, C. A. Bowers, C.P. Fowler, P.B. Schultz, A.D. Hauswirth, T. Weigand, C.T. Miller, Modeling cross model non-Newtonian fluid flow in porous media, Journal of Contaminant Hydrology, 235, 2020, 103708.

[32] M. Anand, J. Kwack, A. Masud, A new generalized Oldroyd-B model for blood flow in complex geometries, International Journal of Engineering Science, 72, 2013, 78-88.

[33] M. Anand, K.R. Rajagopal, A shear-thinning viscoelastic fluid model for describing the flow of blood International Journal of Cardiovascular Medicine and Science, 4(2), 2004, 59-68.

[34] T. Bodnar, A. Sequeira, L. Pirkl, Numerical simulations of blood flow in a stenosed vessel under different flow rates using a generalized Oldroyd-B model, Numerical Analysis and Applied Mathematics, 2, 2009, 645–648.

[35] T. Bodnar, K.R. Rajagopal, A. Sequeira, Simulation of the three-dimensional flow of blood using a shear-thinning viscoelastic fluid model The Mathematical Modelling of Natural Phenomena, 6(5), 2011, 1-24.

[36] T. Bodnar, A. Sequeira, M. Prosi, On the shear-thinning and viscoelastic effects of blood flow under various flow rates, Applied Mathematics and Computation, 217(11), 2011, 5055-5067.

[37] S. Chien, S. Usami, H.M. Taylor, J.L. Lundberg, M.I. Gregersen, Effect of hematocrit and plasma proteins on human blood rheology at low shear rates, Journal of Applied Physiology, 21(1), 1966, 81-87.

[38] J.G. Abuga, T. Chinyoka, Benchmark solutions of the stabilized computations of flows of fluids governed by the Rolie-Poly constitutive model, Journal of Physics Communications, 4(1), 2020, 015024.

[39] J.G. Abuga, T. Chinyoka, Numerical Study of Shear Banding in Flows of Fluids Governed by the Rolie-Poly Two-Fluid Model via Stabilized Finite Volume Methods, Journal of Physics Communications, Processes, 8(7), 2020, 810.

[40] D.V. Boger, Demonstration of upper and lower newtonian fluid behavior in a pseudoplastic fluid, Nature, 265 (1977), pp. 126-128.

[41] L. Pirkl, Numerical Simulation of Incompressible Flows with Variable Viscosity, Diploma Thesis, Czech Technical University of Prague, Faculty of Mechanical Engineering, Department of Technical Mathematics , Prague, 2007.

[42] Jean-Luc Chabert *et. al.*, 1999, A History of Algorithms: From the Pebble to the Microchip, Springer-Verlag.

[43] C. Edwards Jr., 1997, The Historical Development of the Calculus, Springer-Verlag.

[44] E. Turban, J.R. Meredith, 1994 (6th ed.), Fundamentals of management science, Burr Ridge Ill. Irwin.

[45] H.K. Versteeg, W. Malalasekera, 2007, An Introduction to Computational Fluid Dynamics, 2nd. Ed., Pearson Education, England.

[46] K. Sato, A. Yoshitake, Y. Hosoya, H. Mikami, FEM Simulation to Estimate Crashworthiness of Automotive Parts, SAE Technical Paper (No. 982356), SAE

Technical Paper; International Body Engineering Conference & Exposition, Detroit, MI, USA, 1998.

[47] J. Venkatesh, M.P. Murthy, Design and structural analysis of high speed helical gear using Ansys, Int. J. Eng. Res. Appl., 2, 2014, 215-232.

[48] F.T. Johnson, E.N. Tinoco, N.J. Yu, Thirty years of development and application of CFD at Boeing Commercial Airplanes, Seattle. Comput. Fluids, 34, 2005, 1115-1151.

[49] S. Jóczik, Z. Zimborás, T. Majoros, A. Kiss, A Cost-Efficient Approach towards Computational Fluid Dynamics Simulations on Quantum Devices, Appl. Sci., 12, 2022, 2873.

[50] S. Brenner, L. Scott, 1994, The Mathematical Theory of Finite Element Methods, Springer Verlag.

[51] J.L. Favero, A.R. Secchi, N.S.M. Cardozo, H. Jasak, Viscoelastic flow analysis using the software OpenFOAM and differential constitutive equations, Journal of Non-Newtonian Fluid Mechanics, Volume 165, Issues 23–24, 2010, 1625-1636.

[52] S. Chakravarty, P.K. Mandal, A. Mandal, Mathematical model of pulsatile blood flow in a distensible aortic bifurcation subject to body acceleration, International Journal of Engineering Science, 38, 2000, 215–238.

[53] R.N. Pralhad, D.H. Schultz, Modeling of arterial stenosis and its applications to blood diseases, Mathematical Biosciences, 190, 2004, 203–220.

[54] B.K. Mishra, N. Verma, Effects of stenosis on non-Newtonian flow of blood in blood vessels, Australian Journal of Basic and Applied Sciences, 4(4), 2010, 588–601.

[55] D. Srinivasacharya, D. Srikanth, Flow of micropolar fluid through catheterized artery - a mathematical model, International Journal of Biomathematics, 05(02), 2012, 1250019.

[56] D.F. Young, Effect of a time-dependent stenosis on flow through a tube, Journal of Manufacturing Science and Engineering, 90, 1968, 248–254.